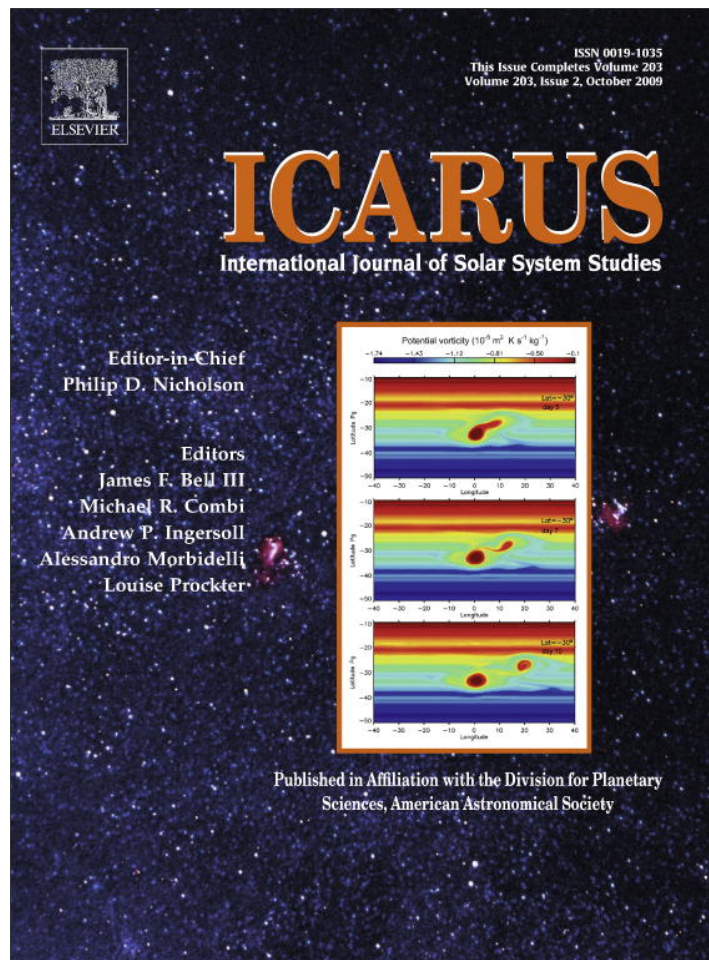


Provided for non-commercial research and education use.
Not for reproduction, distribution or commercial use.



This article appeared in a journal published by Elsevier. The attached copy is furnished to the author for internal non-commercial research and education use, including for instruction at the authors institution and sharing with colleagues.

Other uses, including reproduction and distribution, or selling or licensing copies, or posting to personal, institutional or third party websites are prohibited.

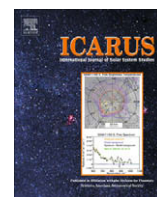
In most cases authors are permitted to post their version of the article (e.g. in Word or Tex form) to their personal website or institutional repository. Authors requiring further information regarding Elsevier's archiving and manuscript policies are encouraged to visit:

<http://www.elsevier.com/copyright>



Contents lists available at ScienceDirect

Icarus

journal homepage: www.elsevier.com/locate/icarus

N-Body simulations of growth from 1 km planetesimals at 0.4 AU

Rory Barnes^{a,b,c,*}, Thomas R. Quinn^a, Jack J. Lissauer^d, Derek C. Richardson^e

^aAstronomy Department, University of Washington, Seattle, WA 98195, USA

^bLunar and Planetary Laboratory, University of Arizona, 1629 E. University Blvd., Tucson, AZ 85721, USA

^cVirtual Planetary Laboratory, USA

^dSpace Science and Astrobiology Division, 245-3, NASA Ames Research Center, Moffett Field, CA 94035, USA

^eDepartment of Astronomy, University of Maryland, College Park, MD 20742, USA

ARTICLE INFO

Article history:

Received 16 April 2008

Revised 23 March 2009

Accepted 25 March 2009

Available online 12 May 2009

Keywords:

Origin, Solar system

Planetesimals

Planetary formation

Earth

ABSTRACT

We present *N*-body simulations of planetary accretion beginning with 1 km radius planetesimals in orbit about a $1 M_{\odot}$ star at 0.4 AU. The initial disk of planetesimals contains too many bodies for any current *N*-body code to integrate; therefore, we model a sample patch of the disk. Although this greatly reduces the number of bodies, we still track in excess of 10^5 particles. We consider three initial velocity distributions and monitor the growth of the planetesimals. The masses of some particles increase by more than a factor of 100. Additionally, the escape speed of the largest particle grows considerably faster than the velocity dispersion of the particles, suggesting impending runaway growth, although no particle grows large enough to detach itself from the power law size-frequency distribution. These results are in general agreement with previous statistical and analytical results. We compute rotation rates by assuming conservation of angular momentum around the center of mass at impact and that merged planetesimals relax to spherical shapes. At the end of our simulations, the majority of bodies that have undergone at least one merger are rotating faster than the breakup frequency. This implies that the assumption of completely inelastic collisions (perfect accretion), which is made in most simulations of planetary growth at sizes 1 km and above, is inappropriate. Our simulations reveal that, subsequent to the number of particles in the patch having been decreased by mergers to half its initial value, the presence of larger bodies in neighboring regions of the disk may limit the validity of simulations employing the patch approximation.

© 2009 Elsevier Inc. All rights reserved.

1. Introduction

The “planetesimal hypothesis” states that planets grow within circumstellar disks via pairwise accretion of small solid bodies known as planetesimals (Chamberlin, 1901; Safronov, 1969; Hayashi et al., 1977). The process of planetary growth is generally divided for convenience and tractability into several distinct stages. In the first stage, microscopic grains collide and grow via pairwise collisions while settling towards the midplane of the disk. If the disk is laminar, then the solids may collapse into a layer that is thin enough for gravitational instabilities to occur (Edgeworth, 1949; Safronov, 1960; Goldreich and Ward, 1973; Youdin and Shu, 2002; Garaud and Lin, 2004; Johansen et al., 2007); such instabilities would have produced planetesimals of ~ 1 km radius at 1 AU from the Sun. If the disk is turbulent, then gravitational instabilities may be suppressed because the dusty layer remains too thick. Under such circumstances, continued growth via binary agglomeration depends upon (currently unknown) sticking and disruption

probabilities for collisions between larger grains (Weidenschilling and Cuzzi, 1993; Weidenschilling, 1995). The gaseous component of the protoplanetary disk plays an important role in this stage of planetary growth (Adachi et al., 1976; Weidenschilling, 1977; Rafikov, 2004).

Once solid bodies reach kilometer-size (in the case of the terrestrial region of the proto-solar disk), gravitational interactions between pairs of solid planetesimals provide the dominant perturbation of their basic Keplerian orbits. Electromagnetic forces, collective gravitational effects, and in most circumstances gas drag, play minor roles. These planetesimals continue to agglomerate via pairwise mergers. The rate of solid body accretion by a planetesimal or planetary embryo is determined by the size and mass of the planetesimal/planetary embryo, the surface density of planetesimals, and the distribution of planetesimal velocities relative to the accreting body. The evolution of the planetesimal size distribution is determined by the gravitationally enhanced collision cross-section, which favors collisions between bodies having smaller relative speeds. Runaway growth of the largest planetesimal in each accretion zone appears to be a likely outcome. The subsequent accumulation of the resulting planetary embryos leads to a large degree of radial mixing in the terrestrial planet region, with

* Corresponding author. Address: Astronomy Department, University of Washington, Seattle, WA 98195, USA.

E-mail address: rory@astro.washington.edu (R. Barnes).

giant impacts probable. Growth via binary collisions proceeds until the protoplanets become dynamically isolated from one another (Lissauer, 1987, 1995).

Numerous groups have attempted to examine the accumulation and dynamics of 1 km planetesimals via numerical simulations. The statistical approach (Greenberg et al., 1978; Kolvoord and Greenberg, 1992) came to be known as the particle-in-a-box (PIAB) method. More recent PIAB investigations, also beginning with 1 km planetesimals, have been performed by Weidenschilling et al. (1997) and Kenyon and Bromley (2006). PIAB assumes that the velocity distribution of planetesimals is a smooth function. Each particle effectively sees a “sea” of particles. The advantage of this model is that one need not sum the gravity between all the bodies; rather, the relative velocities and impact parameters of two colliding particles can be randomly selected from a simple function.

Aarseth and Lecar (1984) were the first to apply N -body modeling to planetary growth with a simulation of 100 lunar-sized bodies that interacted directly and accreted. Computer power and algorithm sophistication increased through the 1990s, but these improvements were not sufficient to enable the direct N -body modeling of growth from 1 km planetesimals. Nevertheless, great strides were made toward understanding the final stages of planet formation (e.g., Agnor et al., 1999; Chambers, 2001; Kokubo and Ida, 2002; Raymond et al., 2006; O’Brien et al., 2006; Morishima et al., 2008). The highest N (the number of particles) simulation to date is that of Richardson et al. (2000), which modeled one million 150 km radius particles for 10^3 years.

In this investigation we simulate 1 km planetesimal growth with an N -body model. Our approach is not to consider an entire disk of planetesimals, as calculating gravitational interactions between more than 1 trillion particles is an intractable task for the foreseeable future. Instead we focus on small, square, shearing patches of the disk, containing up to 10^5 particles. In this way, we follow growth over several orders of magnitude, compare self-consistent and statistical calculations, and lay the groundwork for future investigations of direct simulations of planetesimal growth.

In Section 2, we describe the numerical integration techniques. In Section 3, we summarize the initial conditions of our simulations. In Section 4, we present the results for our baseline model, in which the magnitude of the initial velocity dispersion is equal to the escape speed of 1 km planetesimals. In Section 5, we compare the results of two simulations with different initial velocity dispersions. In Section 6, we discuss some of the key results to emerge from these simulations. Finally, in Section 7, we draw more general conclusions, extrapolate our results to longer times and larger orbital radii, and describe future directions of research. Appendix A lists all symbols and abbreviations used in this article. Appendix B reviews an analytic method for approximating planetesimal accumulation. Appendix C presents three of our simulations to 2000 orbits; these results have been relegated to an appendix because they probably suffer from systematic errors due to the small physical size of the region being simulated combined with the flat slope of the size-frequency distribution of planetesimals at this epoch.

2. Numerical techniques

We use the code PKDGRAV (Richardson et al., 2000; Stadel, 2001; Wadsley et al., 2004) to perform the integrations. This is a parallel, highly scalable N -body algorithm, originally designed for cosmological simulations (see, e.g., Moore et al., 1998). The code incorporates features such as multipole expansions, multistepping, and binary merging to increase speed (described below). Despite these sophisticated techniques, PKDGRAV cannot integrate more

than $\sim 10^5$ colliding 1 km planetesimals for 10^3 years in a reasonable amount of CPU time with our model. Since the collision timescale is of order minutes (see Section 2.3), our “baseline model”, presented in Section 4, required over 4×10^8 timesteps. We describe the equations of motion of the patch in Section 2.1, our collisional model in Section 2.2, the basic principles of PKDGRAV in Section 2.3, the numerical approximations necessary to complete these simulations in Section 2.4, and our methods of verification in Section 2.5.

2.1. Equations of motion

Although carrying out the simulations in a patch greatly reduces N , it adds the new complication of simulating Keplerian shear: we must account for the gradient in the Sun’s gravitational field and the geometry of the disk. If we examine small patches of the disk such that $W \ll r$, where W is the width and length of the square patches and r is the distance from the Sun, then we may approximate quantities, such as surface density, scale height, and circular velocity, as varying linearly in the patch.

Two coordinate systems are used in this model: heliocentric cylindrical and locally Cartesian. The heliocentric system is the more physically meaningful system, as it is based on the geometry of the disk. In these coordinates, the origin is located at the position of the central star, and (r, θ, z) have their standard meanings. We implement the Cartesian system inside the patch, with the origin at the center of the patch. For small θ , these two coordinate systems are related by the following expressions:

$$\begin{aligned} r &= r_{\text{patch}} + x, \\ \theta &= \frac{3}{2}\Omega_{\text{patch}}\frac{x}{r_{\text{patch}}}t + \frac{y}{r_{\text{patch}}}, \end{aligned} \quad (1)$$

where r_{patch} is the heliocentric radius of the center of the patch and Ω_{patch} is the Keplerian orbital frequency of the patch. Essentially the radial direction is mimicked by x and the tangential direction by y . Similarly, the velocities are related by

$$\begin{aligned} \dot{r} &= \dot{x}, \\ \dot{\theta} &= \frac{3}{2}\Omega_{\text{patch}}\frac{x}{r_{\text{patch}}} + \frac{\dot{y}}{r_{\text{patch}}}. \end{aligned} \quad (2)$$

The z -velocities and positions are identical in the two coordinate systems.

For the purpose of the integration, we use the Cartesian system, as outlined in Wisdom and Tremaine (1988), which was based on Hill (1878). The equations of motion inside the patch are

$$\begin{aligned} \ddot{x} - 2\Omega_{\text{patch}}\dot{y} - 3\Omega_{\text{patch}}^2x &= -\frac{\partial\phi}{\partial x}, \\ \ddot{y} + 2\Omega_{\text{patch}}\dot{x} &= -\frac{\partial\phi}{\partial y}, \\ \ddot{z} + \Omega_{\text{patch}}^2z &= -\frac{\partial\phi}{\partial z}, \end{aligned} \quad (3)$$

where ϕ represents the interparticle potentials in the disk. Wisdom and Tremaine assume massless particles ($\nabla\phi = 0$), and provide the general solution

$$\begin{aligned} x &= x_g + A \cos(\Omega_{\text{patch}}t) + B \sin(\Omega_{\text{patch}}t), \\ y &= y_g - \frac{3}{2}\Omega_{\text{patch}}x_g t - 2A \sin(\Omega_{\text{patch}}t) + 2B \cos(\Omega_{\text{patch}}t), \\ z &= C \cos(\Omega_{\text{patch}}t) + D \sin(\Omega_{\text{patch}}t), \end{aligned} \quad (4)$$

where A , B , C , and D are arbitrary constants that correspond to the amplitude of the excursions from a circular, planar orbit, and x_g and y_g are the guiding centers of the epicycles of the particles. The $\frac{3}{2}\Omega_{\text{patch}}x_g$ term is known as the “shear rate” and represents

the Keplerian motion relative to that at $x = 0$. For negative x , the shear rate is positive, as these particles are closer to the star. The y -motion is the tangential motion relative to the center of the patch, not the azimuthal motion of the patch as a whole.

The equations of motion are integrated with a second-order generalized leapfrog scheme derived via the operator splitting formalism of Saha and Tremaine (1992). For the case of orbits in the patch, this integrator prevents secular changes in the guiding center of the epicycle.

2.2. Collision model

Our model assumes perfect accretion. In our implementation, collisions result in one perfectly spherical particle, and all particles have the same density. To conserve angular momentum, the resultant particle receives the net angular momentum of the two colliders (spin plus motion relative to the center-of-mass of the colliding particles), without dissipation (although energy is decreased by 20% during a collision). Our assumption of perfect accretion allows particles to spin faster than break-up, the latter being given by

$$p_{\min} = \sqrt{3\pi/G\rho_{\text{pl}}}. \quad (5)$$

(For a density of 3 g/cm^3 , $p_{\min} = 1.9 \text{ h}$.) Real gravitational aggregates do not merge completely under such circumstances, and hence this assumption will tend to artificially increase planetesimal masses. Conversely, spheres have the smallest possible cross-section for a given volume, so our algorithm is suppressing growth with this approximation. Therefore these two features of our model counteract each other, although we cannot say to what degree they cancel each other out.

The assumption that the particles are always gravitational aggregates may break down during high-energy collisions, in which case fracturing and melting may occur. For tractability, we ignore this possibility. We also ignore any potential radiogenic heating, e.g., by ^{26}Al , as the melting timescale is much longer than the collisional timescale.

2.3. PKDGRAV

PKDGRAV is very efficient because it calculates gravitational forces rapidly. The code works by recursively dividing the physical space, the “domain”, into smaller cells that are organized in a tree. The gravitational forces are then calculated by traversing this tree (e.g., Barnes and Hut, 1986). To calculate the forces on a particle from a given cell, the code determines the apparent size of the cell, that is the angle the cell subtends as viewed from the particle. If this angle is smaller than some minimum angle, Θ , then all moments up to hexadecapole of the particles in the cell are used to calculate the force. Otherwise the cell is opened and the test is repeated on the subcells. This approximation changes the speed of the N -body calculation from $O(N^2)$ to $O(N \log N)$. For further details see Stadel (2001) and Wadsley et al. (2004). For the simulations described here, we used $\Theta = 0.7$ radians.

PKDGRAV also permits the use of periodic boundary conditions, which are required to prevent the patch from self-collapsing. To do this, each patch is reproduced 8 times, in the form of “ghost cells” that completely surround the actual patch in the x - and y -directions. Eq. (4), however, also requires that particles in the ghost cells move at the appropriate shear velocity. The centers of the ghost cells therefore move in the y -direction as prescribed by Eq. (4).

Gravity calculations per time interval are minimized by a multistep algorithm. Multisteping divides the base timestep into smaller intervals. For our simulations the timestep is based on the largest acceleration a particle feels at each timestep. In this algo-

rith isolated planetesimals move at the base timestep, t_{base} , set to about 100 steps per orbit. As particles approach each other their timesteps drop to a minimum value, until they either miss or collide. Each smaller timestep is a factor of 2 shorter than the previous in order to keep all of the base gravitational kicks commensurate. Typically 95% of particles are on the longest timestep, but we still resolve all collisions.

Two timescales are relevant in this problem, the orbital time and the crossing time of two particles that just miss. The orbital period, P , is of order one year, but the crossing time is of order minutes. For two particles of radius R to just miss, on a parabolic orbit, the crossing time is

$$t_{\text{cross}} = r/v_{\text{esc}} = \frac{R}{\sqrt{\frac{8\pi}{3}G\rho R^2}} = \sqrt{\frac{3}{8\pi G\rho}}, \quad (6)$$

and is therefore independent of the masses. In this scenario and with densities of 3 g/cm^3 , the crossing time is 772 s. P and t_{cross} determine t_{base} and t_{min} , the maximum and minimum possible timesteps. To be conservative (note that the version of PKDGRAV employed in this investigation does not integrate Eq. (3) symplectically), we set these values as

$$t_{\text{base}} = \eta P \quad (7)$$

and

$$t_{\text{min}} = \eta t_{\text{cross}}, \quad (8)$$

where η is a scale factor, chosen such that the integrals of motion are constant to a satisfactory degree. Convergence tests showed that for the systems we consider, $\eta = 1/300$ provided the necessary accuracy. The number of available timesteps, ζ , is

$$\zeta = 1 + \log_2 \left(\frac{t_{\text{base}}}{t_{\text{min}}} \right). \quad (9)$$

At 0.4 AU and $\rho = 3 \text{ g/cm}^3$, this translates to $\zeta = 14$.

2.4. Numerical approximations

Although PKDGRAV is fast relative to other integration techniques, we must make several additional approximations in order for the simulation to be practical, and to appropriately model equation (3). These approximations do not alter the physics appreciably, and resulted in nearly a factor of 10 speed-up.

As mentioned above, the timestep for each particle is determined by its current acceleration, which is a function of the local mass density. Particles on large timesteps are not close to other particles and cannot be close to collision. We therefore set a ceiling for timesteps to search for collisions. This small modification increases speed by a factor of 2–3 depending on the surface density of the patch (and hence the local density).

Occasionally during the evolution of the patches, binaries (gravitationally bound pairs of particles) form. This is a natural result of 3-body encounters. Although it is preferable to allow these binary systems to evolve normally, they often become stuck in the shortest timesteps, greatly diminishing the advantage of multisteping. Therefore, we artificially merge them. In our simulations, binary merging accounts for about 0.01% of all merging events and therefore this small change in the total energy of the simulation should be negligible. Simulations of globular clusters have shown that tight binaries tend to get tighter during a 3-body encounter, and loose binaries tend to become looser (Heggie, 1975). To make binary merging as realistic as possible we therefore also require the eccentricity of the particles involved to be less than 0.9, so that wide binaries may still be disrupted.

2.5. Verification

Given the complexity of this problem (non-inertial frame, large range of growth, and numerical approximations), we need to quantify the accuracy of our methodology. The patch framework provides some inherent tests, but we must also understand the statistics of the problem; this patch is supposed to be a representative piece of a much larger annulus of material. At some point, the number of particles drops to a sufficiently small number that the results cannot be trusted. In this subsection we describe our methodology for verifying the results presented in Sections 4 and 5.

In the shearing model, the particles are in a non-inertial frame. Therefore the integrals of motion normally associated with dynamics (momentum, energy, angular momentum), are not directly applicable. In this formalism there are two constants of motion we use to check the validity of these simulations. In the nomenclature of Wisdom and Tremaine (1988), these conserved integrals are

$$u \equiv \frac{\sum_{l=1}^N m_l \frac{dx_l}{dt}}{M_{\text{patch}}}, \quad (10)$$

$$w \equiv \frac{\sum_{l=1}^N m_l \left(\frac{dy_l}{dt} + \frac{3}{2} \Omega_{\text{patch}} x_l \right)}{M_{\text{patch}}},$$

where M_{patch} is the total mass in the patch. These parameters essentially correspond to the center of mass velocity. For this situation, the center of mass should remain motionless; we need to verify that u and w remain much less than the random velocities. Note that our definition includes the masses of the particles, whereas the Wisdom and Tremaine (1988) definition did not, as they weighted all particles equally.

Eq. (10) would be sufficient if we were integrating particles without growth, which we are not. The patch model at least requires that no particle is dominant. Therefore a zeroth order requirement is that no particle reaches a mass equal to that of the sum of the remaining particles. This constraint, however, fails to take into account how the most massive particles alter the dynamics of the disk. As a typical particle passes by the largest mass particle, it receives a kick, and energy associated with Keplerian motion may be transformed into the random motions of the swarm, increasing the velocity dispersion, i.e., “viscous stirring” (Wetherill and Stewart, 1989). Afterward that increase in random velocity should be damped down by subsequent interactions with other typical particles. To verify that no particles grow so large as to dominate the stirring in the patch, we consider the ratio of the gravitational stirring of the largest particle to the sum of all other particles:

$$S \equiv \frac{m_{\text{max}}^2}{\sum_{l \leq l_{\text{max}}} N_l m_l^2 - m_{\text{max}}^2} \quad (11)$$

(Lissauer and Stewart, 1993). Exactly how large S can grow is not clear *a priori*, but values below ~ 0.1 should be satisfactory.

Should the mass distribution in the patch suggest that significantly massive planetesimals are present in the disk, but not present in a patch, then the patch is not modeling a large enough region of the disk. We check this possibility by plotting $m^2 N_k$ as a function of m , where N_k is the number of particles in mass bin $k \equiv m/m_1$. We will see in Section 4.4.2 and Appendix C that unmodeled large bodies are likely to become a problem as our model evolves.

A final point of concern is the size of the epicycles of particles compared to the size of the patch. Should the eccentricity of a particle grow large enough that the radial excursions ($2ae$, where a is semi-major axis, e is eccentricity) exceed the size of the patch, then we may not be sampling the region appropriately. We parameterize this effect as

$$\beta \equiv \frac{2r_{\text{patch}} e}{W}, \quad (12)$$

where W is the patch width. The equations of motion do not depend on eccentricity, so there are no numerical problems if this occurs, only concerns about the physical interpretation of this phenomenon. Our choice of W is very small compared to the size of the terrestrial annulus. As long as β remains less than or close to unity, the radial mixing throughout the disk is negligible, and our interpretations are independent of the particles' eccentricity. Only if β grows to large values is there cause for alarm. We focus on the second largest β value, as occasional strong kicks could temporarily result in large eccentricities for one particle.

3. Initial conditions

We assume a surface density of 37.2 g/cm^2 at 0.4 AU , 30% higher than predicted by the minimum mass solar nebula model (Hayashi, 1980), but consistent with previous studies (Richardson et al., 2000). The bulk density of the planetesimals, ρ_{pl} , is taken to be 3 g/cm^3 . The mass of a planetesimal with $R = 1 \text{ km}$ is thus

$$m_{\text{pl}} = \frac{4\pi}{3} \rho_{\text{pl}} R^3 = 1.26 \times 10^{16} \text{ g}. \quad (13)$$

Assuming the surface density of the disk scales as $\Sigma \propto a^{-1}$, the number of planetesimals in the annulus $0.4 \text{ AU} \leq a \leq 2.5 \text{ AU}$ is

$$N = \frac{M_{\text{ann}}}{m_{\text{pl}}} = 3.5 \times 10^{12}. \quad (14)$$

As we are unable to directly integrate trillions of particles, we must reduce N to a tractable value by dividing the disk into patches.

Most of our simulations begin with the root mean squared (RMS) velocity dispersion, v_{RMS} , set to the escape speed of 1 km planetesimals, v_{esc} (Safronov, 1969; Stewart and Wetherill, 1988). This relationship assumes that the system is relaxed, which may or may not be the case depending on the processes and timescales to form planetesimals. This RMS speed is the magnitude of the random motion of the particles, but it is not distributed isotropically due to the 2:1 axis ratio of the epicycle; instead the distributions are described by

$$v_x = \sqrt{\frac{2}{3}} v_{\text{esc}}, \quad (15)$$

$$v_y = v_z = \frac{1}{\sqrt{6}} v_{\text{esc}}$$

(Binney and Tremaine, 1994). For a radius of 1 km and $\rho_{\text{pl}} = 3 \text{ g/cm}^3$ particles, v_{esc} is 1.29 m/s .

From this velocity distribution, we calculate the equilibrium vertical density profile of the disk. To do this we assume the disk is in a state of hydrostatic equilibrium; the “pressure” of the vertical component of the velocity distribution maintains its thickness. The vertical component of solar gravity increases linearly with distance from the midplane, therefore the density follows a Gaussian profile,

$$\rho = \rho_0 e^{-\frac{z^2}{2Z_0^2}}, \quad (16)$$

where ρ is the density, ρ_0 is the density at the midplane, and Z_0 is the scale height of the disk. The (Gaussian) scale height is determined by the z -velocity distribution, the mass of the central star and the orbital radius. Hydrostatic equilibrium allows a calculation of the scale height:

$$Z_0 = \sqrt{\frac{v_z^2 r^3}{2GM_\odot}} = \sqrt{\frac{v_z^2}{2\Omega_z^2}}. \quad (17)$$

The scale height also depends on the self-gravity of the planetesimal disk. To compensate for this, we implement a “vertical frequency enhancement” to simulate an infinite plane sheet of matter so that

$$\Omega_z = \Omega_{\text{patch}} + \sqrt{\frac{2\pi GM_{\text{patch}}}{W^3}}. \quad (18)$$

The second term in Eq. (18) is an analytic restoring force that simulates the disk's self-gravity and reduces Z_0 . For our baseline model (Simulation L_1 presented in Section 4), Ω_z is 0.2% larger than Ω_{patch} .

Our nomenclature for simulations is based on the relative size and the initial dynamical state. L stands for “large”, M for “medium” and S for “small”. The subscript is the ratio of the initial velocity dispersion to the escape speed of a 1 km planetesimal. In Table 1, we present the initial conditions for these simulations.

We assume that scattering is very effective, and that gas drag is negligible. Simulations L_1 , M_1 and S_1 presume the planetesimals are in a form of equilibrium. However, there remain many unknowns in the formation of these planetesimals and variations of a factor of 2 are plausible. We therefore ran two integrations with non-equilibrium initial conditions. We integrated one system that began with $v_{\text{RMS}} = 0.5v_{\text{esc}}$ (Simulation $M_{0.5}$), and one with $v_{\text{RMS}} = 2v_{\text{esc}}$ (Simulation M_2). In these simulations the scale height was set by Eq. (17). These two simulations are presented in Section 5.

Each of the simulations was run at least until the number of bodies in the patch has been halved, $t_{1/2}$. This time is related to the mean free time, τ , between collisions, which can be approximated as

$$\tau \approx \frac{m_1}{\rho_0 \sigma_{\text{pl}} v_{\text{RMS}}} \approx t_{1/2}, \quad (19)$$

where σ_{pl} is the gravitational cross-section, $\sigma(1 + v_{\text{esc}}^2/v_{\text{RMS}}^2)$, and ρ_0 is given by

$$\rho_0 = \frac{\Sigma}{\sqrt{2\pi}Z_0}. \quad (20)$$

Eq. (19) is only valid at the midplane at time $t = 0$. The density changes with z , and v_{RMS} change with time. Nonetheless, this simple model provides valuable insights into the dynamics. For the initial conditions we use, $\tau \approx 500$ orbits.

Richardson et al. (2000) modeled a planetesimal disk with 10^6 particles, but they simulated a later stage of planetary growth in which the collision rate was much lower than it is here. Therefore, our integrations proceed slower, even with the advanced methodologies described in Section 2.3. If we set $N_{\text{patch}} \sim 10^5$, then the simulations are large, but we may still examine several different initial conditions. We choose a square patch of width $W = 10^{-3}r_{\text{patch}}$ for our largest simulation, L_1 . In our model, this choice corresponds to an initial N of 106,130, a small enough number to be tractable, but large enough to be statistically significant. Note, however, that the medium-sized simulations have dimensions $W = 5 \times 10^{-4}r$, and the small one $W = 2.5 \times 10^{-4}r$. These cases run faster, and are included to test various assumptions in the baseline case.

Table 1
Initial conditions of the patch simulations.

ID	N	v_{RMS} (m s ⁻¹)	Z_0 (km)	ρ_0 (10 ⁻⁷ g/cm ³)
L_1	106,130	1.29	475	3.1
M_1	26,532	1.29	475	3.1
S_1	6633	1.29	475	3.1
$M_{0.5}$	26,532	0.65	237	6.3
M_2	26,532	2.6	950	1.6

4. The baseline model

The simulations of our baseline model (those with subscript 1) begin with 1 km radius particles with an RMS velocity equal to that of the escape speed of 1 km particles with a density of 3 g/cm³. From this dispersion the initial scale height is set by Eq. (17). The simulation with the most particles, L_1 , required 354 orbits (89.6 years) to halve the total number of particles. The M_1 and S_1 simulations required 349 and 361 orbits, respectively, to reach $t_{1/2}$. In this section we describe the results of these three simulations. Table 2 summarizes some of the results of our simulations at $t_{1/2}$. At this time, the patch is nearing a condition in which it is too small to correctly model the velocity distribution (see Section 4.4.2); results of these simulations beyond $t_{1/2}$ are presented in Appendix C.

4.1. Mass growth

The mass spectra of Simulations L_1 , M_1 , and S_1 at 100, 200, 300 and 354 orbits ($t_{1/2}$ for L_1) are plotted in Fig. 1. Fig. 2 shows the (differential) mass distributions with logarithmic bins of size $2^l m_1$, $l = 1, 2, 3, \dots$, i.e., the first bin contains all particles of mass m_1 , the second bin contains particles of $2m_1$ and $3m_1$, the third bin contains particles in the range $4m_1 \leq m \leq 7m_1$, etc. The histograms shown in Fig. 2 appear to follow a power law size distribution. The one apparent exception is the single particle in the largest bin for L_1 at $t_{1/2}$, which is detached by one bin from the remaining particles (the “swarm”). However, upon closer inspection, this particle has a mass of 275 m_1 , whereas the second and third largest particles have masses of 122 and 116 m_1 , respectively. All three of these particles just miss being members of the 128–255 m_1

Table 2
Results of 1 km planetesimal growth at 0.4 AU at $t_{1/2}$.

ID	$t_{1/2}$ (orbits)	m_{max} (m_1)	v_{RMS} (m s ⁻¹)	F_g	P_{peak} (h)
L_1	354	276	1.93	20.2	1.05
M_1	349	142	1.89	13.7	1.05
S_1	361	73	1.95	9.2	1.05
$M_{0.5}$	253	202	1.86	17.8	1.65
M_2	542	47	2.41	4.8	0.65

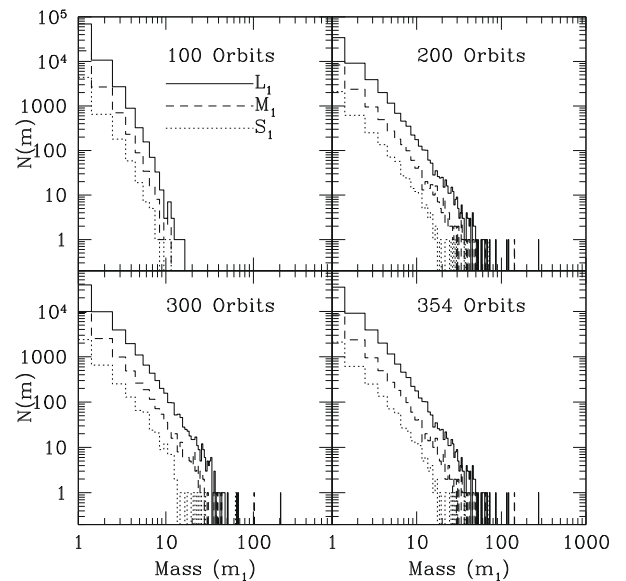


Fig. 1. The semi-log (differential) mass distributions for Simulations L_1 (solid line), M_1 (dashed line) and S_1 (dotted line) after 100 orbits (top left), 200 orbits (top right), 300 orbits (bottom left) and 354 orbits (bottom right).

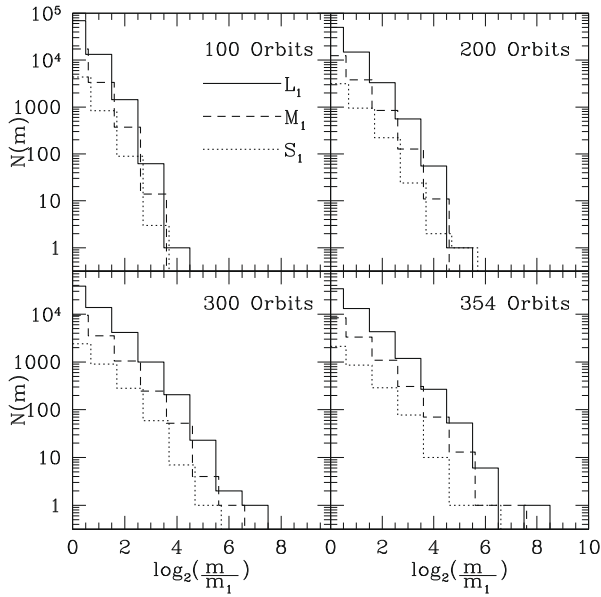


Fig. 2. The log–log (differential) mass distributions of Simulations L_1 (solid line), M_1 (dashed line) and S_1 (dotted line) at 100 orbits (top left), 200 orbits (top right), 300 orbits (bottom left), and 354 orbits (bottom right). Note that the M_1 simulation data have been offset to the right by 0.1 and the S_1 data by 0.2 in order to improve readability.

bin. Therefore, the distributions presented in Fig. 2 suggests that runaway growth has *not* occurred.

To further examine the nature of the mass distribution, we matched the mass distribution to single parameter fits. We consider a power law,

$$N(k) \propto k^{-b}, \quad (21)$$

and an exponential,

$$N(k) \propto e^{-k/c}. \quad (22)$$

We fit the constants b and c by using the line method to minimize χ^2 (Press et al., 1996) with one sigma uncertainties assumed to be $\sqrt{N_k + .75} + 1$. For small N_k this gives a better approximation to the distribution of χ^2 for sparsely sampled data (Gehrels, 1986), e.g., some bins at large k have zero particles. The fits are constrained so that the total mass is the same as in the simulation, and the number of degrees of freedom is approximately equal to m_{\max}/m_1 . We must take into consideration the fact that the first bin is unusual in that all the particles were originally in that bin. Therefore we also consider fits that exclude the data at $m = m_1$. These fit parameters are denoted with a prime. We found that exponential fits are always poor, so we will focus on the power law fits.

In Fig. 3 we show the mass distributions of Simulations L_1 (top), M_1 (middle) and S_1 (bottom), with the analytic fits for comparison at each simulation's $t_{1/2}$. The values of all the fit parameters are presented in Table 3. In that table we see that the values of unreduced χ^2 are all significantly better when the first data point is excluded. All fits include the large-mass particles and we conclude that these largest particles do not represent a new class (i.e., runaway growth has not occurred). Note that forcing the fitted distribution to contain the same total mass as the simulation forces the exponential cases to converge to poor fits.

In Fig. 4 we compare the merger rate ($-dN/dt$) of Simulation L_1 with that predicted by the mean free time of the patch. The prediction comes from the following relation

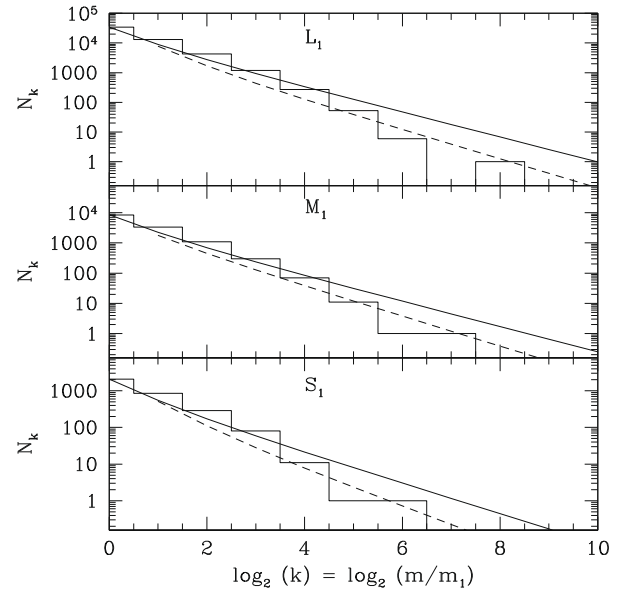


Fig. 3. Comparison of the mass distributions at $t_{1/2}$ for the baseline simulations. The histograms represent the mass distribution at each model's value of $t_{1/2}$ and the straight lines are the power law fits, solid includes the first bin, dashed does not.

Table 3

Fit parameters of the mass distributions at $t_{1/2}$.

ID	b	χ_b^2	b'	$\chi_{b'}^2$	c	χ_c^2	c'	$\chi_{c'}^2$
L_1	2.39	1693	2.62	376	1.3	6224	1.9	1690
M_1	2.39	894	2.64	168	1.2	1400	1.9	853
S_1	2.38	492	2.65	107	1.3	1073	1.9	308
$M_{0.5}$	2.4	307	2.59	74	1.2	1723	2	466
M_2	2.38	489	2.61	154	1.3	1440	1.7	189

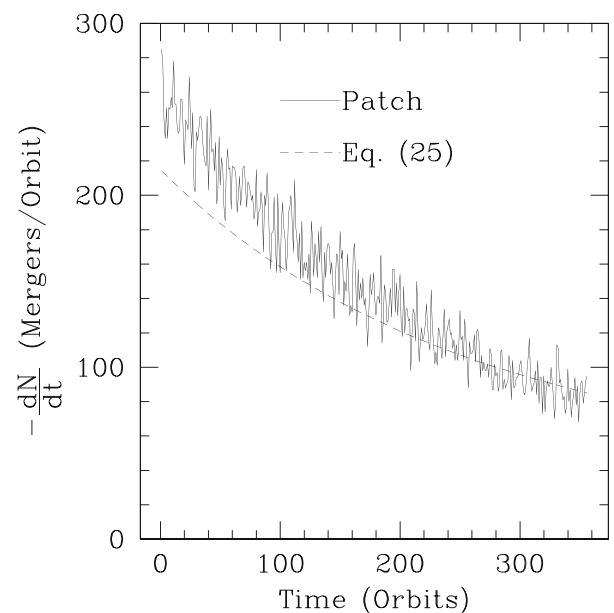


Fig. 4. The evolution of the merger rate of Simulation L_1 . The solid line is that observed in the patch (sampled once per orbit), and the dashed line is that predicted by the mean free time of the patch (recalculated each orbit from the instantaneous values of v_{RMS} , $\langle \sigma_{\text{pl}} \rangle$, ρ_0 and $\langle m \rangle$) in Simulation L_1 .

$$\frac{dN}{dt} = -\frac{N\rho_0\langle\sigma_{pl}\rangle v_{RMS}}{\langle m \rangle}, \quad (23)$$

where the brackets indicate quantities averaged over the entire swarm. We assume the cross-section to be the gravitationally enhanced area of two particles with the average radius. The right-hand side of Eq. (23) is the number of particles divided by the mean free time. Initially the mean free time argument underpredicts the merger rate and later it is about right. Overall this simplified estimate of the merger rate remains near the actual value. The rate is dropping because the total number of particles in the patch is decreasing due to merging.

Next we compare our results to that of the constant, linear, and product solutions to the coagulation equation (Wetherill, 1990; see also Appendix B) in Simulation L₁. These three solutions are relatively simple compared to more recent derivations (see e.g., Kenyon and Luu, 1998; Kenyon and Bromley, 2004). However, the recent models do not provide analytic solutions for the number of particles in each mass bin (see Eqs. (B9), (B10) and (B12)). We find the three collisional probability coefficients (see Eqs. (B6)–(B8)) have values of $v_1 = 5.3 \times 10^{-8}$, $v_2 = 1.84 \times 10^{-8}$, and $v_3 = 2.65 \times 10^{-8}$ for Simulation L₁.

In Fig. 5 we plot the growth of some of the largest masses in Simulation L₁ through 354 orbits. Also shown are the predicted largest masses from the three solutions to the coagulation equation, with collisional probabilities that are constant as a function of time, and equal to the values listed above. The growth in our N-body model follows the product solution to the coagulation equation for about 250 orbits, but then the two diverge as the N-body model predicts faster growth. This divergence is probably a result of the product solution's failure to conserve mass for $t > t_{1/2}$. At $t_{1/2}$ the largest particle has a mass of 276 m_1 . Nonetheless, the agreement over the majority of the simulation suggests that even the Wetherill (1990) product coagulation model is a reasonable representation of early growth of planetesimals.

In Fig. 6 we further compare Simulation L₁ to the Wetherill (1990) models. The six panels examine six different ranges of k . For mass ranges, the predicted number of particles is determined by summing all mass bins in that range. From this figure we see that no solution to the coagulation fits the data over all values of

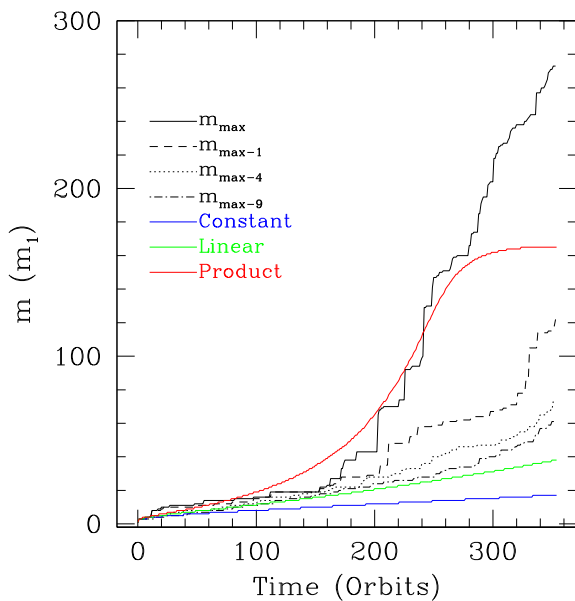


Fig. 5. The evolution of the largest, second largest, fifth largest and tenth largest masses in Simulation L₁. The solid red line corresponds to m_{max} in the product solution to the coagulation equation, green to the linear, and blue to the constant.

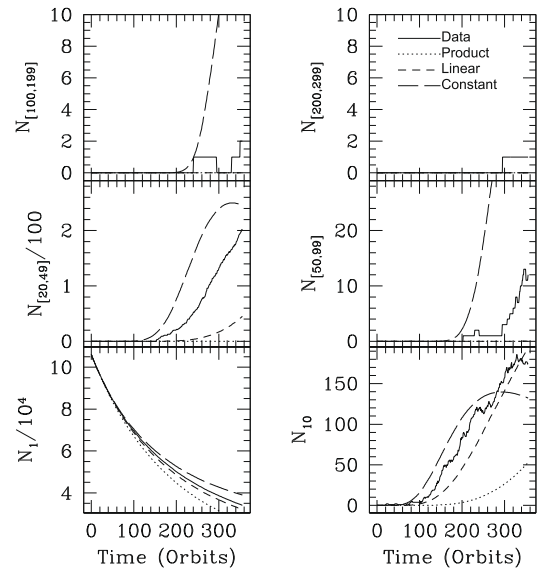


Fig. 6. A comparison of the distribution of masses in Simulation L₁ with those predicted by coagulation theory for 6 different mass ranges: $k = 1$ (bottom left), $k = 10$ (bottom right), $20 \leq k < 50$ (middle left), $50 \leq k < 100$ (middle right), $100 \leq k < 200$ (top left) and $200 \leq k < 300$ (top right).

k . At low masses ($k \lesssim 10$), the linear solution is the best-fit to the data, but at larger masses the product solution is better. However, at these larger values of k , the product solution still differs from the actual distribution by more than a factor of 2.

4.2. Velocity dispersion

Fig. 7 shows the evolution of the RMS velocity of all particles, the escape speed of the largest particle, and the escape speed of the average-mass particle in Simulation L₁. The velocity dispersion slowly grows to a value of $\sim 2 \text{ m s}^{-1}$ at $t_{1/2}$ (which is evidence of viscous stirring), while the escape speed of the largest particle grows to a value of 8.4 m s^{-1} . At $t_{1/2}$ the largest body has a mass

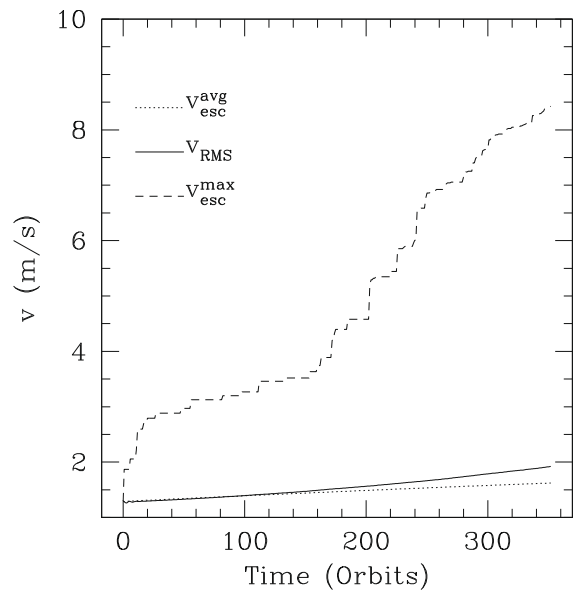


Fig. 7. The evolution of the RMS velocity of the patch (solid line), the escape speed of the largest particle (dashed line) and the escape speed of the mean particle (dotted line) in Simulation L₁.

of $m_{\max} = 276m_1$ and a radius of 6.5 km. From these values we can identify the gravitational focusing factor for the largest body, the ratio of its gravitational cross-section to its geometrical cross-section. This factor is

$$F_g = 1 + \frac{2Gm_{\max}}{v_{\text{RMS}}^2 R_{\max}} = 1 + \left(\frac{v_{\text{esc}}}{v_{\text{RMS}}}\right)^2. \quad (24)$$

The final values of F_g for Simulations L_1 , M_1 , and S_1 are 20.2, 13.7, and 9.2, respectively (see Fig. 8).

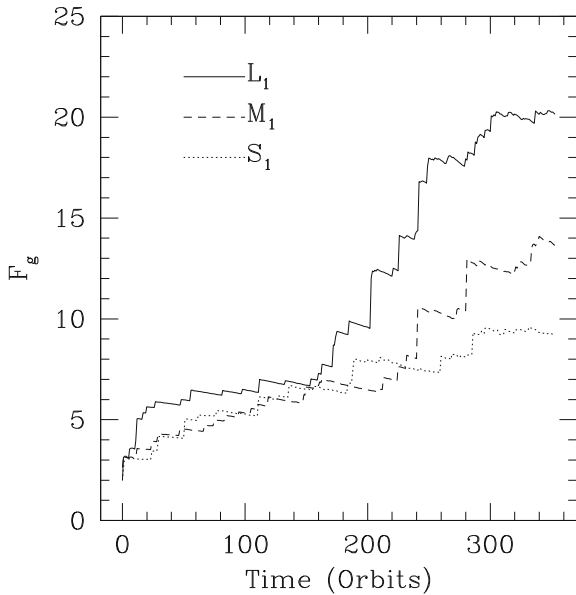


Fig. 8. Evolution of the gravitational focusing factor of the most massive particle in Simulations L_1 (solid line), M_1 (dashed line), and S_1 (dotted line). In larger simulations the focusing grows larger because the biggest particles are more massive, but the velocity dispersions are about equal in the three simulations (see Table 2).

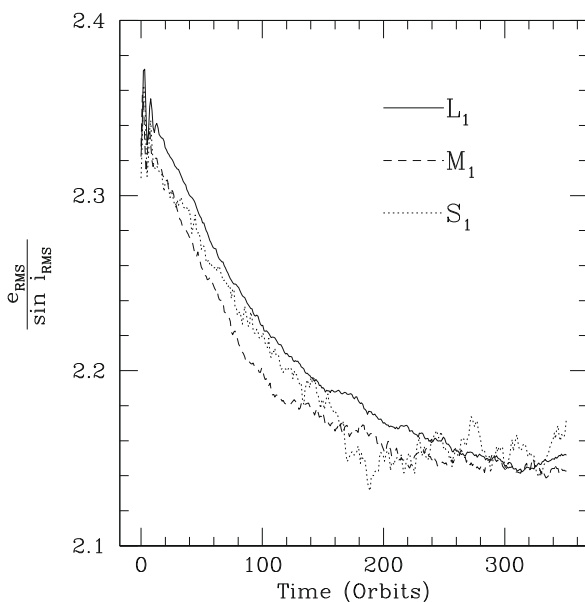


Fig. 9. Evolution of $e_{\text{RMS}} / \sin i_{\text{RMS}}$ for Simulations L_1 (solid line), M_1 (dashed line), and S_1 (dotted line). The values drop from ~ 2.35 to ~ 2.15 over ~ 200 orbits. At that time the ratios level out, which suggests the initial conditions were not in equilibrium.

We evaluate the ratios of e_{RMS} to $\sin i_{\text{RMS}}$ in Fig. 9. (Note the inclinations are in a regime such that the difference between $\sin i$ and i is about 1 part in 10^{10} .) The ratios begin at 2.35 but drop to ~ 2.15 , similar to previous results (Greenzweig and Lissauer, 1990; Kokubo and Ida, 1996).

We investigate the role of dynamical friction by examining e_{RMS} and i_{RMS} as a function of mass at $t_{1/2}$. For each populated bin, we computed these values (if only one body occupied a bin we used its e and i values), and show the results in Fig. 10. As expected, larger masses are dynamically colder than smaller masses, nonetheless, they have greater energy, implying that equipartition of energy is not achieved.

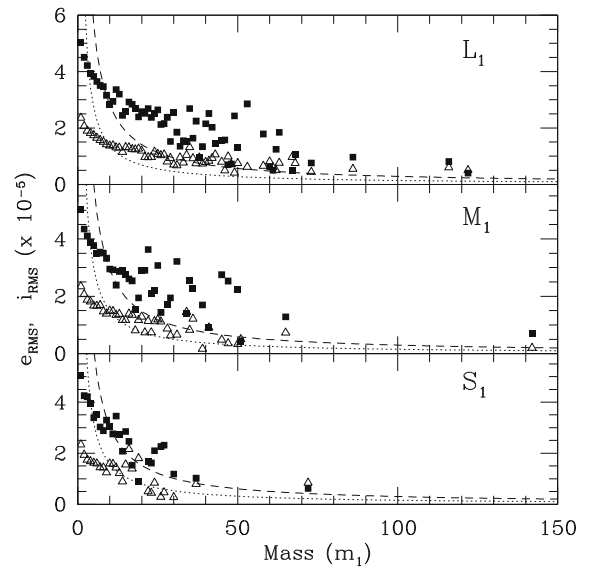


Fig. 10. The values of e_{RMS} and i_{RMS} as a function of mass at $t_{1/2}$ for the three equilibrium simulations. Filled squares represent eccentricity, open triangles inclination. In the L_1 simulation, the largest mass planetesimal ($275m_1$) is not shown; its values are $e = 2.6 \times 10^{-6}$ and $i = 1.8 \times 10^{-7}$. For reference, the dashed line represents equipartition of energy in e , dotted in i , normalized to the values for $k = 10$.

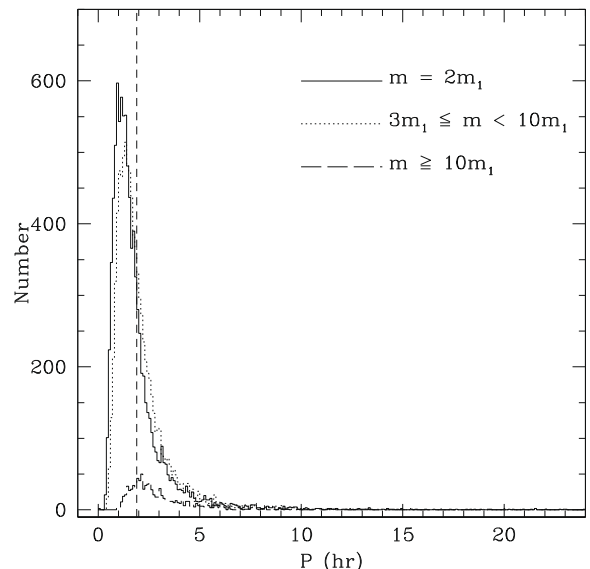


Fig. 11. The final spin (at $t_{1/2}$) periods for the planetesimals in Simulation L_1 . The dashed vertical line represents the minimum period of a gravitational aggregate.

4.3. Rotation rates

We plot the rotation periods of all planetesimals in Simulation L_1 with $m > m_1$ at $t_{1/2}$ in Fig. 11. Only 14 bodies had periods longer than 1 day. Recall that initially all planetesimals have no spin. We plot the spin distribution over three mass ranges: $m = 2m_1$, $3m_1 \leq m < 10m_1$, and $m \geq 10m_1$. The peak period is at 1.05 h, which is less than the minimum period for a spherical gravitational aggregate of density 3 g/cm^3 , see Eq. (5). Thus, this distribution suggests that our assumption (which is the standard one) of completely inelastic collisions resulting in mergers overestimates planetesimal growth rates.

4.4. Accuracy tests

In this subsection we quantify the accuracy of our results (see Section 2.5). Section 4.4.1 measures the numerical accuracy of our code, and Section 4.4.2 describes the statistical accuracy of our method.

4.4.1. Numerical accuracy

In Fig. 12 we examine the validity of Simulation L_1 by plotting u and w . These parameters measure the center-of-mass motion of the patch. Both u and w remain less than 0.1 cm s^{-1} , about 1000 times smaller than the typical random velocities in the patch and about 10^5 times smaller than the shear rate across the patch, $\Omega W = 4720 \text{ cm s}^{-1}$. We therefore conclude that this variation is tolerable (Wisdom and Tremaine, 1988).

4.4.2. Statistical accuracy

Although Simulation L_1 contains a large number of particles (relative to modern N -body simulations), it still represents a very small fraction of the terrestrial annulus. We therefore must characterize the robustness of our results. The most critical aspect of this experiment is the mass of the largest particle. Should a particle reach a large enough mass that it inappropriately dominates the dynamics of the patch, then our assumptions have broken down.

First we consider β , Eq. (12), which measures the radial excursions of particles, see Section 2.5. We find that after 354 orbits of Simulation L_1 that $\beta_{\text{max}-1}$ (the second largest value) is still well be-

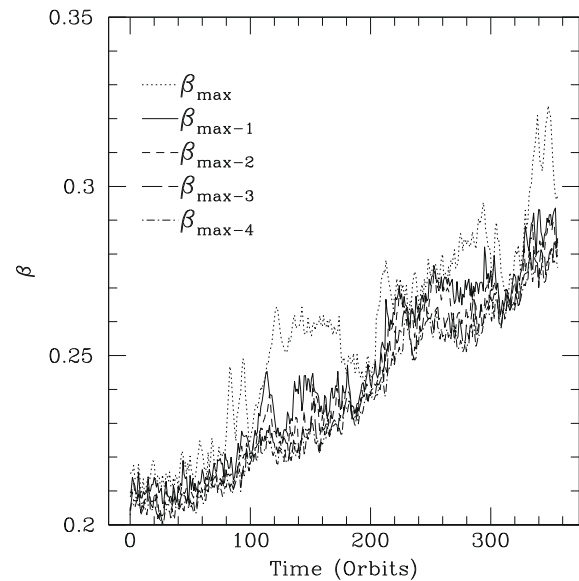


Fig. 13. The growth of the five largest values of β in Simulation L_1 as a function of time. All values lie well below unity, indicating that no particle's epicycle is larger than the width of the patch.

low unity (Fig. 13). Therefore, the patch size for Simulation L_1 passes this requirement.

In Fig. 14, we plot the evolution of the stirring efficiency S (Eq. (11)) in the three baseline simulations. At $t_{1/2}$ the largest particle is about one-eighth as effective at stirring as the rest of the swarm in Simulation L_1 , about one-seventh in M_1 , and nearly one-fifth in S_1 . These values suggest we are nearing a situation in which the statistical accuracy of this simulation cannot be confirmed, but such a situation has not occurred yet.

Next we evaluate the distribution of $m_k^2 N_k$ as a function of mass. This quantity measures how effective each mass bin is at stirring the patch. As described in Section 2.5, the distribution can reveal the possibility of large-mass bodies beyond the boundaries of the patch that could significantly change the dynamical character of the planetesimal swarm. For this model, after about $t_{1/2}$ there is

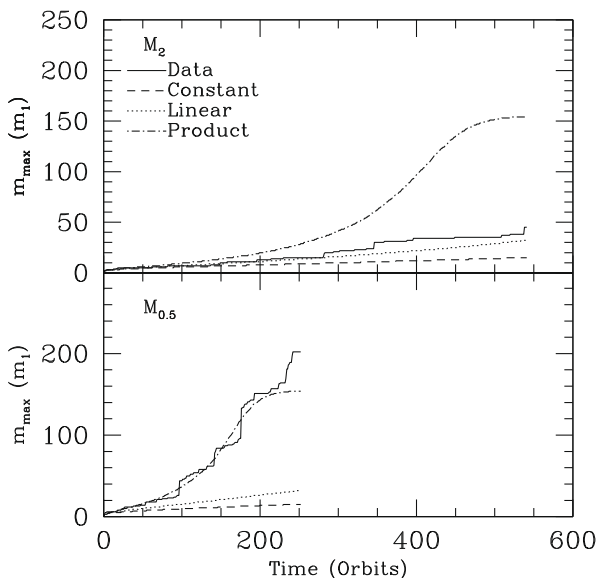


Fig. 12. The evolution of the constants of motion in Simulation L_1 . The values of u and w vary at a level 3 orders of magnitude below that of the random motions.

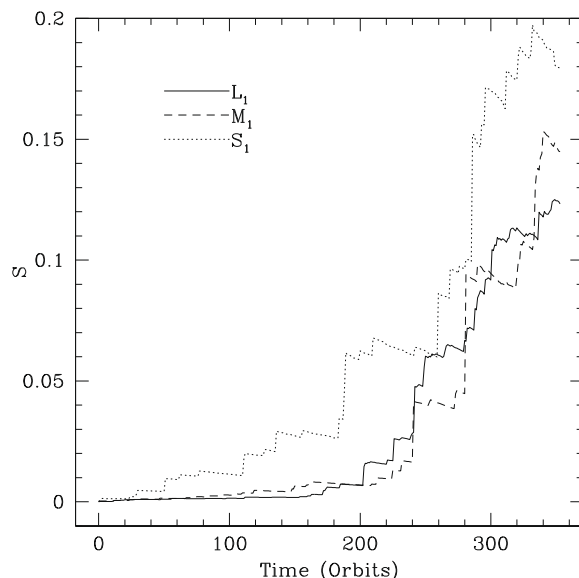


Fig. 14. The stirring efficiency of the largest particles in Simulation L_1 (solid line), M_1 (dashed line), and S_1 (dotted line) relative to the rest of their respective swarms.

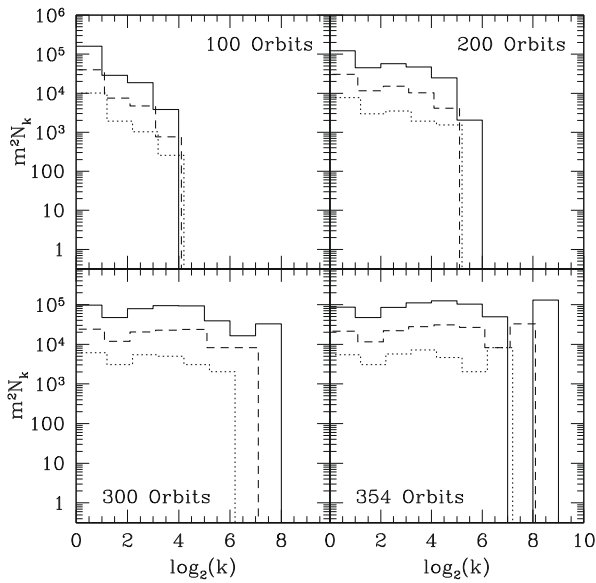


Fig. 15. The stirring power of particles as a function of mass at 100 orbits (top left), 200 orbits (top right), 300 orbits (bottom left), and 354 orbits ($t_{1/2}$ for Simulation L_1 ; bottom right). The solid line represents Simulation L_1 , dashed M_1 , and dotted S_1 . After 354 orbits, the slopes are roughly flat; this shows that our patches might not be large enough to contain a statistically significant number of particles. Note that the Simulation M_1 data are offset by 0.1, and the S_1 data by 0.2.

a significant chance that large perturbers are close enough to affect the patches' dynamics. In Fig. 15 we plot $m^2 N_k$ vs. $\log m$ at four times. If $m^2 N_k$ is decreasing as a function of mass near the upper end of the mass distribution, then the patch is large enough to be a statistically representative piece of the annulus, and the velocity distribution of the patch should be close to that of the disk. If, alternatively, the distribution is increasing, then there exist nearby large particles that could dominate the stirring. We see at $t_{1/2}$ the distribution is flat, suggesting we have reached the limit of our model. These curves suggest that results at later times may be inaccurate, hence our decision to exile those data in Appendix C.

5. Alternative velocity distributions

In this section we describe the results of two simulations that begin with different initial velocity dispersions than the baseline model. The results of these simulations may be important since the initial velocity dispersion of planetesimals is ill-constrained. Earlier growth may occur too rapidly for the velocity dispersion to equilibrate ($v_{\text{RMS}} = v_{\text{esc}}$). We thus explore a range of initial velocity dispersions. These simulations also show how sensitive the results of Section 4 are to variations in the initial velocity dispersions. In Simulation $M_{0.5}$ the initial velocity dispersion is set to $0.5v_{\text{esc}}$, in Simulation M_2 it is set to $2v_{\text{esc}}$.

For Simulations $M_{0.5}$ and M_2 , $t_{1/2}$ occurred after 253 and 542 orbits, respectively. Figs. 16 and 17 show the mass distributions at $t_{1/2}$ for each of these models. As expected, when the velocity dispersion is smaller, accretion proceeds faster, due to the increased gravitational focusing. Moreover, the largest particles have a greater accretion advantage and so are more massive at $t_{1/2}$ in $M_{0.5}$ than in M_2 .

In Fig. 17 we show how our power-law fits (both with and without the $k = 1$ data) to the log-log mass distribution, Eq. (21), compare to the actual distributions at each simulation's $t_{1/2}$. As with the baseline models (see Fig. 3), the exponential fit has a much larger unreduced χ^2 value. The best fit parameters for these two simulations at time $t_{1/2}$ are listed in Table 3.

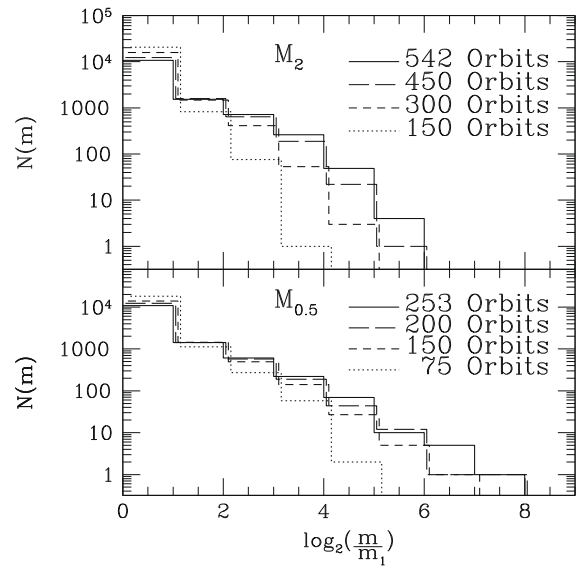


Fig. 16. The mass functions of the non-equilibrium runs as a function of time. The earliest time is offset to the right by 0.05, the next time is offset by 0.1, etc. Larger initial velocity dispersion suppresses runaway growth. These plots can be compared to Fig. 2.

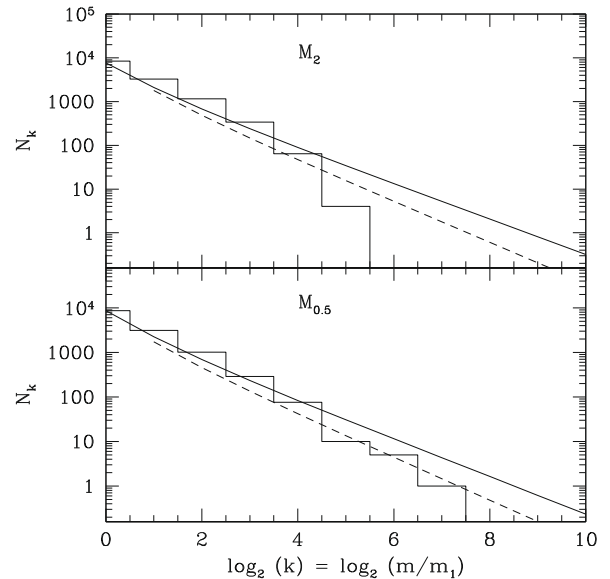


Fig. 17. Comparisons of the mass distributions at $t_{1/2}$ for Simulations M_2 (top) and $M_{0.5}$ (bottom) and the best power law fits to the data, Eq. (21). The histograms are the mass distributions from the simulations, the straight lines are the fits (solid includes first bin, dashed does not).

We continue by plotting the evolution of the largest mass particle for each non-equilibrium run in Fig. 18. As in Fig. 5, we also include the predictions of the Wetherill (1990) model. The linear solution is a good fit to the distribution of Simulation M_2 , while the product solution appears to be a good fit to that of Simulation $M_{0.5}$.

In Fig. 19 we plot the evolution of the velocity dispersions. In the top panel (Simulation M_2), we see that the velocity dispersion actually drops initially, but then increases similarly to the other runs. This decrease results from the inelastic nature of the collisions, as well as, to a lesser degree, the deposition of translational kinetic energy into rotational kinetic energy. However, we interpret this result with caution due to potential inconsistencies in

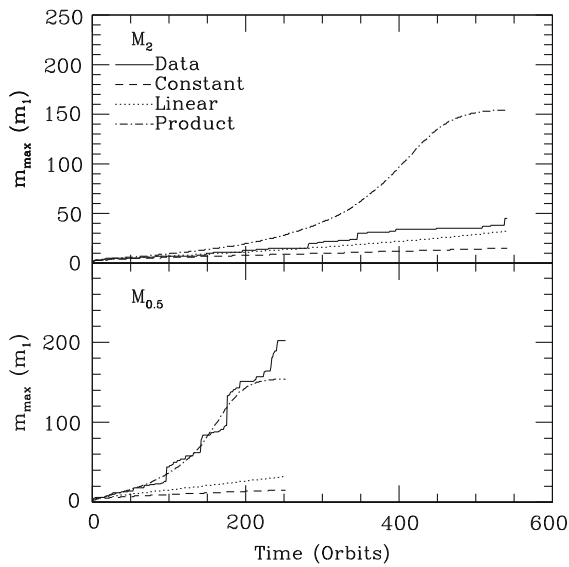


Fig. 18. The growth of the largest mass in each model as a function of time, and the predictions of the constant, linear, and product solution of the coagulation equation.

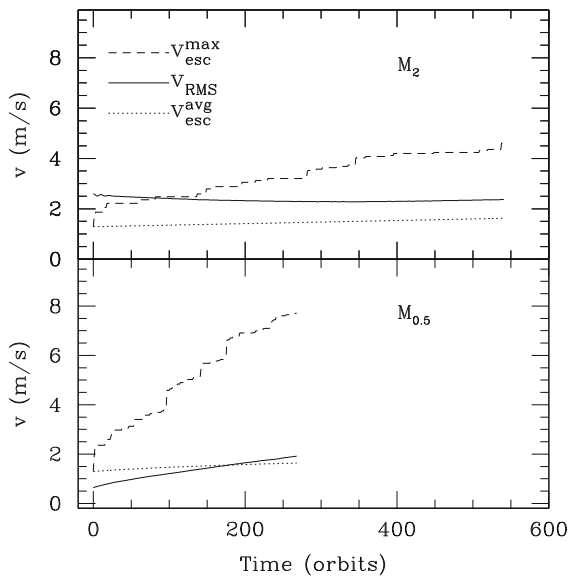


Fig. 19. The evolution of the velocity dispersions in the non-equilibrium simulations. In Simulation M_2 (top panel), the dispersion actually drops toward equilibrium. The final values of v_{RMS} are close to 2 m s^{-1} , as in the baseline case.

the perfect accretion model (see Section 2.2). When the initial velocity dispersion is too low, the dispersion quickly rises (compare to Fig. 7). The final values of F_g are 17.8 and 4.8 for Simulations $M_{0.5}$ and M_2 , respectively. As with the baseline models, equipartition of energy has not occurred in these simulations.

In Fig. 20 we plot the final spin distributions for the non-equilibrium patches. The peaks lie below the minimum gravitational aggregate period. Simulation M_2 consists of especially fast rotators, due to a larger amount of kinetic energy of random motion available for transformation into rotational energy.

6. Discussion

Several results stand out in Sections 4 and 5. First is that runaway growth has not begun to occur for any particle in any simu-

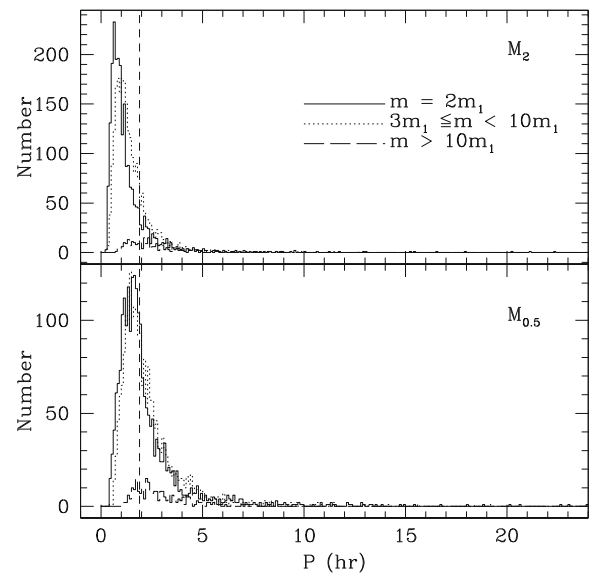


Fig. 20. The final spin distributions for merged particles for the non-equilibrium simulations. The vertical dashed line is the minimum period as defined by Eq. (5). For Simulation M_2 very few particles have periods in excess of 10 h, but Simulation $M_{0.5}$ has several long-period planetesimals.

lation. Second, the velocity dispersions of the patches remain close to the escape speed of the average-mass particle. Third, the growth rate is moderately sensitive to the initial velocity dispersion; changes of a factor of 2 in the initial RMS velocity can excite or retard the early growth rate of the most massive particles. Fourth, our collision model (Section 2.2) is too simplified in that it assumes spherical particles experiencing perfect accretion. Fifth, some aspects of the coagulation equation model the growth well, but discrepancies of at least a factor of 2 are present, and the best model (linear or product) appears to depend on the initial value of v_{RMS} . Sixth, the power law fits represent a realistic model of the actual mass distribution.

We present a summary of the results in Tables 2 and 3. Comparing Simulation M_1 to the alternate-RMS velocity trials, we see that its final properties lie between those of Simulations $M_{0.5}$ and M_2 . Therefore, m_{max} and $t_{1/2}$ depend upon the initial velocity dispersion in a systematic manner.

Growth proceeds easily in all our models, despite no initial seed. There is some indication from the final mass distributions that the annulus will develop particles with a mass in excess of $10^4 m_1$ by $t_{1/2}$. By considering the stirring effects as a function of mass we have found that by $t_{1/2}$ such large bodies could significantly modify the dynamical properties of our patches. Therefore, in order to continue our integrations further, we must consider a larger patch, such that the curve of S vs. m turns over. Our simulations do not show how much larger the patch must be, or indeed if any patch is adequate and N -body simulations at later times must model a full annulus. Inconsistencies between our N -body integration and the Wetherill (1990) model rule it out to estimate the mass distribution. We note, however, that more complicated models (e.g., Kenyon and Bromley, 2004) may make a better match to our calculations, but the development and implementation of such models was beyond the scope of this investigation. We encourage future statistical researchers to use our results to verify their collision kernels.

In Fig. 21 (see also Figs. 7 and 19) we examine the different evolutions of the RMS velocity dispersion for all our simulations. In each case, viscous stirring increases the velocity dispersion. Moreover, all have $v_{RMS} \approx 2 \text{ m s}^{-1}$ at $t_{1/2}$. Note that at $t_{1/2}$ the average mass is $2m_1$, which corresponds to an escape speed of 1.7 m s^{-1} .

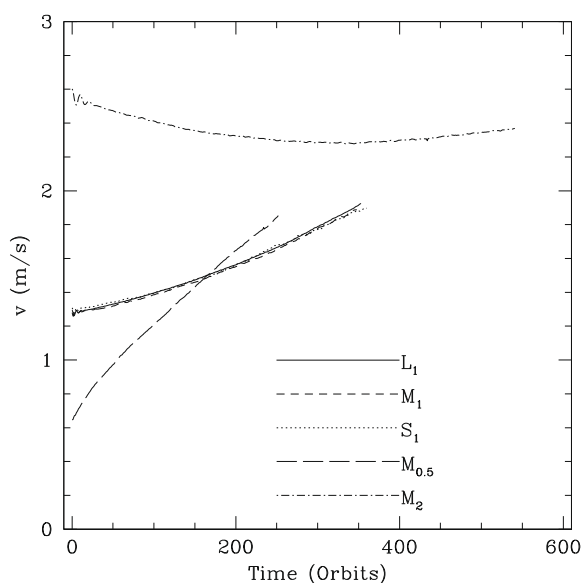


Fig. 21. Evolution of all RMS velocities.

This equivalence suggests that, at least early on, the velocity dispersion grows at approximately the same rate as the escape speed of the typical mass particle.

The perfect accretion model has produced several results that may be spurious. The sum of all these issues, in our implementation, is that orbital angular momentum is too easily transferred into rotational angular momentum, and produces spin rates that are too high (see Figs. 11 and 20). Therefore the spin distributions presented here should not be regarded as physically realistic, and the mass distributions of our simulations should be considered upper bounds.

Assuming the initial swarm of planetesimals is composed of gravitational aggregates, we need larger simulations with a more realistic collisional model (see Leinhardt and Richardson, 2005) in order to determine the true nature of the post-collision particles. Presumably angular momentum is lost by shedding rubble from the surface. Three possibilities await this freed rubble: collision with other planetesimals, orbital migration via gas drag into the central star, or recollapse into 1 km planetesimals (Goldreich et al., 2004). Given the number density of planetesimals at this stage of growth, the former seems the most likely. This limitation of our model demonstrates the need to perform similar simulations with a more realistic collisional model (e.g., Leinhardt and Richardson, 2005; Leinhardt et al., 2009).

Our analytic fits to the mass distributions show that exponential fits do not match the data (see Table 3). However, a power law does provide a reasonable fit for most of our models. Removing the $k = 1$ bin from our fits results in a significant decrease in the unreduced χ^2 values, as shown in Table 3. We conclude that runaway growth has not begun in our simulations.

All of our simulations show that growth from 1 km planetesimals can proceed quickly. In fact, it proceeds so rapidly that our model breaks down in just a few hundred orbits (see Section 4.4.2, Fig. 15). Therefore the only way to realistically proceed beyond $t_{1/2}$ is to enlarge our patches. As we expand our patches, the number of particles increases. Given that Simulation L₁ required $\sim 30,000$ node hours to complete on the Columbia Supercomputer at NASA Ames, and computation time scales as $N \log N$, we may not be able to expand our patches such that they are both statistically accurate and computationally tractable. Our results therefore suggest that the patch model may be inadequate to model later stages of terrestrial planet formation.

7. Conclusions

We have performed the first N -body simulations of growth from 1 km planetesimals. The initial conditions of our runs were chosen to be similar to those believed to have existed in our protosolar disk; substantially different parameters may be appropriate for the initial stages of growth in extreme exoplanetary systems (Lissauer and Slartibartfast, 2008). These simulations required hundreds of thousands of node hours of supercomputer time, using an advanced N -body code designed specifically to examine systems with large N . Although numerous shortcuts and approximations were incorporated in our model, we believe that our results provide insights into planetesimal growth and lay a foundation for future investigations.

Planetesimal growth from a uniform swarm of 1 km-sized planetesimals proceeds in a stochastic fashion. Our results have confirmed some of the trends seen in the semi-analytical research (Greenberg et al., 1978; Wetherill, 1990; Weidenschilling et al., 1997) into the growth of 1 km planetesimals. Until more realistic models of fragmentation can be implemented in N -body codes, statistical methods are the only feasible approach to address fragmentation.

Some of the assumptions of our model broke down relatively quickly, demonstrating the limits of the patch approximation in modeling planetary accretion. Nonetheless, our results suggest new directions of research for this epoch of planet formation. In particular, a more realistic collisional model (one in which additional small particles carry away excess angular momentum, i.e., fragmentation) seems most important. Such a model may suppress growth (as well as eliminating unphysical spins), and hence planetesimals would not grow so quickly. However, this approach is considerably more complex and numerically intensive than those presented here. Until these modifications can be made, our results represent the most accurate model of 1 km planetesimal growth available.

Acknowledgments

We thank Richard Greenberg, Glen Stewart, Don Brownlee, Guillermo Gonzalez, Paul Hodge, and Brian Jackson for useful discussions, and an anonymous referee for valuable suggestions. This research was funded primarily by NASA's Terrestrial Planet Finder Foundation Science/Solar System Origins under Grant 811073.02.07.01.15. Simulations were performed on the Lemieux supercomputer at the Pittsburgh Supercomputer Center and the Columbia supercomputer at NASA Ames Research Center. Computers used to analyze these simulations were provided by the University of Washington's Student Technology Fund. Parallel code development was partly supported by NSF Grant PHY-0205413. Rory Barnes also thanks KFB for his unwavering encouragement, and acknowledges additional support from NASA's Planetary Geology and Geophysics Grant NNG05GH65G and NASA's Graduate Student Research Program. Thomas Quinn was partly supported by the NASA Astrobiology Institute. Jack J. Lissauer acknowledges support from NASA's PG&G program, Grant 811073.02.01.01.12. Derek C. Richardson acknowledges support from NASA Grant NAG511722 issued through the Office of Space Science.

Appendix A. List of symbols and abbreviations

A	arbitrary constant
A_{ij}	collisional probability coefficient in coagulation theory
a	semi-major axis
B	arbitrary constant
b	power law fit parameter

b'	power law fit parameter with $m = m_1$ bin excluded
C	arbitrary constant
c	exponential fit parameter
c'	exponential fit parameter with $m = m_1$ bin excluded
D	arbitrary constant
e	eccentricity
e_{RMS}	root mean square eccentricity of particles in a patch
F_g	gravitational focusing factor
f	fraction of particles relative to initial number
G	Newton's gravitational constant
i	inclination
i_{RMS}	root mean square inclination of particles in a patch
j	counter in coagulation equations
k	ratio of particle mass to mass of 1 km planetesimal
k_R	mass of a runaway particle relative to a 1 km planetesimal
L_1	Largest baseline simulation
l	counter in coagulation equations
l_{max}	largest value of counter l
$M_{0.5}$	simulation with the initial velocity dispersion magnitude set to half that of Simulation L_1
M_1	medium-sized baseline simulation
M_2	simulation with the initial velocity dispersion magnitude set to twice that of Simulation L_1
M_{ann}	mass in an annulus of the protoplanetary disk
M_{patch}	total mass inside a patch
M_{\odot}	mass of the Sun
M_{\oplus}	mass of the Earth
m	mass
m_1	mass of 1 km planetesimal
m_{crit}	particle mass at which, in one orbit, it collides with an equal mass of gas
m_{max}	largest mass in a simulation
$m_{\text{max}-1}$	second largest mass in a simulation
$m_{\text{max}-4}$	fifth largest mass in a simulation
$m_{\text{max}-9}$	tenth largest mass in a simulation
m_{pl}	mass of planetesimal
$\langle m \rangle$	average mass of planetesimals
N	number of bodies in a simulation
N_0	initial number of planetesimals in a simulation
N_{patch}	number of bodies in a patch
N_k	number of bodies in a mass bin
n_k	number density of particles in mass bin k
P	orbital period
P_{peak}	peak of the spin period distribution
S_1	Simulation with same initial properties as L_1 , but only 1/16 the size
PIAB	particle-in-a-box
R	planetesimal radius
R_{max}	radius of largest planetesimal
r	heliocentric radius
r_{patch}	heliocentric radius of the center of a patch
S	stirring power of largest mass relative to that of all other bodies
S_1	smallest-sized baseline simulation
t	time
$t_{1/2}$	the time required to reduce the total number of particle at distance r by 2
t_{base}	longest timestep in a simulation
t_{cross}	crossing time for two planetesimals
t_{min}	minimum timestep in a simulation
u	center-of-mass speed of a patch in the x -direction
V	volume
v	velocity
v_{esc}	escape speed of a planetesimal
v_{RMS}	root mean square speed of a patch
v_x	speed in x -direction
v_y	speed in y -direction
v_z	speed in z -direction
W	size scale of a patch

w	center-of-mass speed of a patch in the y -direction
x	Cartesian coordinate that mimics heliocentric distance
x_g	x position of guiding center of a planetesimal's epicycle
y	Cartesian coordinate that mimics azimuthal position
y_g	y position of guiding center of a planetesimal's epicycle
z	height above/below midplane
Z_0	scale height of planetesimal disk
β	radial excursions of a planetesimal due to eccentricity
β_{max}	largest radial excursion of a particle in a patch
$\beta_{\text{max}-1}$	second largest radial excursion in a patch
$\beta_{\text{max}-2}$	third largest radial excursion in a patch
$\beta_{\text{max}-3}$	fourth largest radial excursion in a patch
$\beta_{\text{max}-4}$	fifth largest radial excursion in a patch
ζ	number of rungs in a simulation
η	scale factor to determine timesteps
Θ	maximum apparent size of a cell for PKDGRAV to only use the hexadecapole moment
θ	azimuthal position of a planetesimal in heliocentric coordinates
v_1	collisional probability coefficient in constant solution of coagulation equation
v_2	collisional probability coefficient in linear solution of coagulation equation
v_3	collisional probability coefficient in product solution of coagulation equation
ρ	volume mass density
ρ_0	volume mass density at midplane
ρ_{pl}	mass density of a planetesimal
Σ	surface density
Σ_0	coefficient that scales surface density of planetesimal disk
σ	physical cross-section of a planetesimal
σ_{pl}	gravitationally enhanced cross-section of a planetesimal
$\langle \sigma_{\text{pl}} \rangle$	average gravitationally enhanced cross-section of planetesimals
τ	mean free time between planetesimal physical collisions
ϕ	gravitational potential
χ_b^2	unreduced χ^2 value for power law fit to mass distribution
$\chi_b'^2$	unreduced χ^2 value for power law fit to mass distribution with $m = m_1$ mass bin excluded
χ_c^2	unreduced χ^2 value for exponential fit to mass distribution
$\chi_c'^2$	unreduced χ^2 value for exponential fit to mass distribution with $m = m_1$ mass bin excluded
Ω_{patch}	Keplerian orbital frequency of a patch
Ω_z	vertical frequency due to Keplerian motion and the mass of the disk

Appendix B. The coagulation equation

Here we summarize the basics of the coagulation equation as presented by Wetherill (1990). The discrete form of the coagulation equation is

$$\frac{dN_k}{dt} = \frac{1}{2} \sum_{l+j=k} A_{lj} n_l n_j - n_k \sum_{l=1}^{\infty} A_{lk} n_l, \quad (\text{B1})$$

where the generic indices j , k and l are just the ratio m/m_1 . In Eq. (B1), N_k is the number of particles in bin k , A_{jl} is the probability of collision, n_j is the total number density of particles of mass j , m is the mass, and m_1 is the mass of a 1 km planetesimal. The first term is the collision probability of all combinations of particles of mass l and j that sum to equal the current mass bin k . The mass bin is the quantum of the mass spectrum. The factor of 1/2 prevents the summation from counting all collisions twice (when $l = j$). The second term is the loss of particles from mass bin k to larger mass bins.

Note that, despite the discrete nature of Eq. (B1), for $t > 0$, it can predict a fractional number of particles in each bin.

The collisional probability coefficient, A_{ij} , is a function of the relative velocity of particle i to j , their masses, the number density of each bin, and the volume being considered. Therefore

$$A_{ij} = A_{ij}(v_{\text{rel}}, m_i, m_j, n_i, n_j), \quad (\text{B2})$$

where n_i (n_j) is the number density of particles with mass i (j). Three forms of this function have been examined. The simplest solution is

$$A_{ij} = v_1, \quad (\text{B3})$$

a constant. For linear dependence we assume

$$A_{ij} = v_2(l + j), \quad (\text{B4})$$

a constant times the sum of the masses, and the dependence on velocities and densities has been subsumed into v_2 . These two possible solutions both fall under the category of orderly growth. A third solution, which is proportional to the product of the masses, assumes

$$A_{ij} = v_3lj. \quad (\text{B5})$$

At any given orbit, Wetherill also gives equations for the collisional probabilities as a function of time:

$$v_1 = \frac{2(1-f)}{N_0 t}, \quad (\text{B6})$$

$$v_2 = -\frac{\log f}{N_0 t}, \quad (\text{B7})$$

and

$$v_3 = \frac{2(1-f)}{N_0 t}. \quad (\text{B8})$$

The solutions to the constant and sum forms are

$$N_k = N_0 f^{2k} (1-f)^{k-1}, \quad (\text{B9})$$

and

$$N_k = N_0 \frac{k^{k-1}}{k!} f(1-f)^{k-1} e^{-k(1-f)}, \quad (\text{B10})$$

respectively, where N_0 is the initial number of particles, and f is just the fraction of the number of particles remaining at time t ,

$$f = \frac{N_{\text{tot}}(t)}{N_0} = \frac{\sum_{l=1}^{\infty} N_l}{N_0}. \quad (\text{B11})$$

The product solution to the coagulation equation is

$$N_k = N_0 \frac{(2k)^{k-1}}{k!k} (1-f)^{k-1} e^{-2k(1-f)}, \quad (\text{B12})$$

and yields runaway growth. This, however, leads to the natural problem that a runaway particle is a special particle, and it should not be treated as typical. This marks the breakdown of the PIAB model. These solutions to the coagulation equation are used in Section 4. In the text we refer to Eq. (B9) as constant coagulation, Eq. (B10) as linear coagulation, Eq. (B12) as product coagulation.

Appendix C. The baseline model to 2000 orbits

In the spirit of Icarus' flight to the Sun, we present results for the baseline simulations from $t_{1/2}$ to 2000 orbits here. As shown in Section 4.4.2, after $t_{1/2}$ larger mass bodies may significantly alter the velocity dispersion in the patches. However, the locations of such particles relative to the patch are unknown. The synodic period across the radial width of the patch is about 2400 orbits. We may therefore presume that by 2000 orbits, a large mass has entered the patch and significantly altered the dynamics, but the time

Table 4

Results of 1 km planetesimal growth at 0.4 AU after 2000 orbits.

ID	$m_{\text{max}}(m_1)$	v_{RMS} (m s^{-1})	F_g	P_{peak} (h)
L ₁	5879	7.94	9.69	0.85
M ₁	4117	7.89	7.95	0.75
S ₁	773	6.00	4.95	0.85

and magnitude of the changes are unknown. Although the results in this appendix suffer from significant inconsistencies, we nonetheless present them here, as they represent the only N -body simulation of growth from 1 km planetesimals to date. Table 4 lists some of the properties of the baseline models at 2000 orbits. Results in this appendix should not be regarded as physically realistic simulations of planetesimal growth beyond $t_{1/2}$!

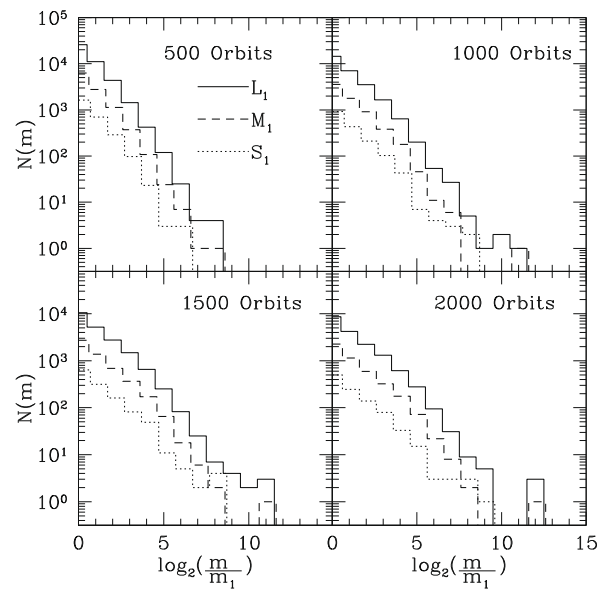


Fig. 22. Mass spectrum at various times during the evolution of the baseline patches in log-log format. Note that the M₁ simulation has been offset by 0.1 and S₁ by 0.2.

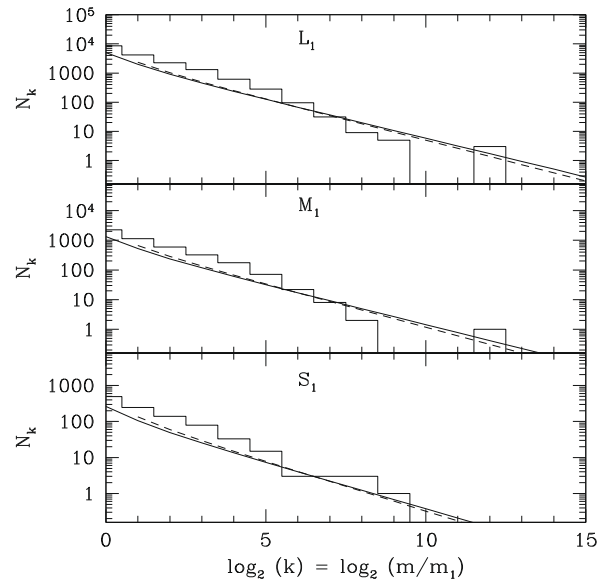


Fig. 23. The mass function of Simulations L₁ (top), M₁ (middle) and S₁ (bottom) and the associated power-law fits to the data; see Eq. (21) and Table 5.

Fig. 22 presents the mass distribution of particles in a format similar to Fig. 2. At 2000 orbits, three particles in L_1 and one in M_1 have reached masses larger than $5000 m_1$. By comparison, the fourth largest planetesimal in L_1 is one-sixth as massive, $814 m_1$, see Fig. 24.

Fig. 23 presents the mass functions at 2000 orbits, along with the associated analytic fits to the data. At 2000 orbits the power law has become a better fit to the data than at $t_{1/2}$. Table 5 lists the fit parameters (and corresponding measures of goodness of fit) at 2000 orbits. The values of the key parameters b and b' all cluster near 1.9. At 2000 orbits the exclusion of the $k = 1$ bin does not cause dramatic changes in the unreduced χ^2 values, which is not surprising since only 10% of the particles remain at $k = 1$.

Fig. 24 shows the evolution of some of the largest particles in the L_1 patch. At 713 orbits, the two largest particles in the patch merge to form a $1610 m_1$ mass object. This merger has important consequences for our assumptions about the statistical accuracy of our patch, as shown below.

In Fig. 25 we show the evolution of v_{RMS} compared to the escape speed of the largest and typical particle in Simulation L_1 . After 500 orbits, v_{RMS} appears to grow linearly, while $v_{\text{esc}}^{\text{max}}$ begins to level off (except for the major merger event at 716 orbits). These qualitatively different growth rates suggest that the larger particles are beginning to significantly heat the patch. Note that even this dynamical heating is probably an underestimate, as particles outside the patch with larger mass should have sheared into this patch by 700 orbits.

We compare RMS velocity and mass growth for the three baseline runs in Fig. 26. The RMS velocities remain close to each other up to $\sim t_{1/2}$ (top panel), but subsequently diverge. This divergence corresponds with the masses of the largest particles in L_1 and M_1

Table 5
Fit parameters of the mass distributions at 2000 orbits.

ID	b	χ_b^2	b'	$\chi_{b'}^2$	c	χ_c^2	c'	$\chi_{c'}^2$
L_1	1.88	486	1.93	253	8.0	11,562	10.2	4511
M_1	1.89	141	1.96	71	7.4	2783	9.8	1029
S_1	1.85	31	1.91	20	7.9	560	10.0	206

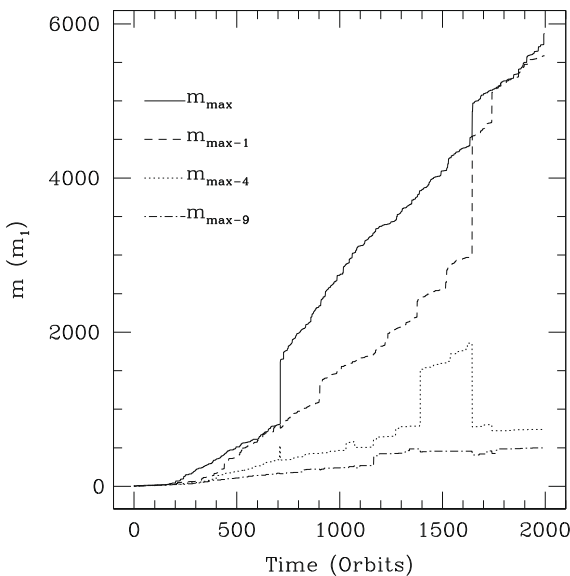


Fig. 24. Evolution of some of the most massive particles in the L_1 run. Note the merger of two $\sim 800 m_1$ objects at 713 orbits. The three largest particles end up with masses in excess of $5000 m_1$.

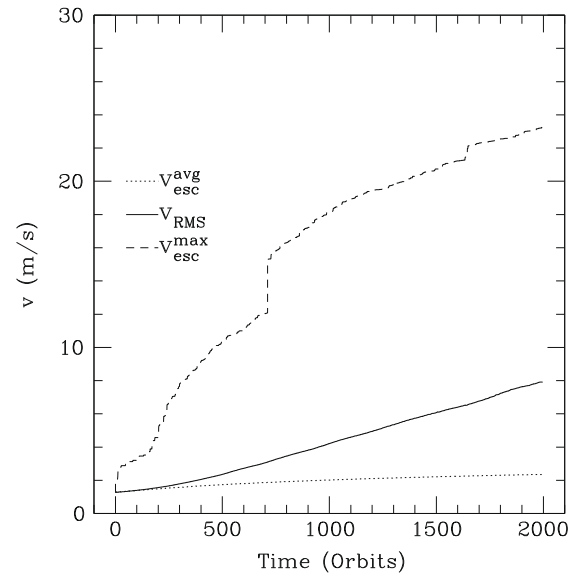


Fig. 25. Evolution of the escape speed of the largest particle (dashed line), RMS velocity (solid line), and escape speed of the average mass particle (dotted line) for Simulation L_1 .

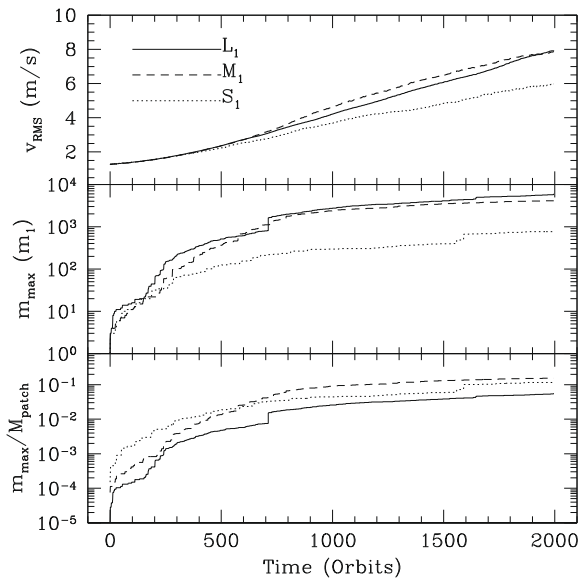


Fig. 26. Top: Evolution of the RMS velocities for the three baseline models. The values for Simulations L_1 and M_1 stay relatively close to each other, but the S_1 value remains lower. Middle: Comparison of the growths of the largest particles in the baseline simulations. The largest particles in L_1 and M_1 remain within about a factor of 2 of each other, while the largest particle in S_1 lags by about an order of magnitude after 1000 orbits. Bottom: Fraction of the patch mass absorbed into the largest particle. At all times, the fractions remain within a factor of a few of each other.

reaching $100 m_1$. Note that Simulation M_1 has the highest velocity dispersion from 615 to 1939 orbits. This feature occurs because the largest particle in M_1 is nearly as large as that in L_1 (middle panel), but since the M_1 patch is smaller than L_1 , the largest particle in M_1 contains a larger fraction of the patch mass (bottom panel), and is therefore a more effective stirrer (see below). Although the largest particle in Simulation S_1 contains approximately the same fraction of the total mass as the particles in the other patches, its actual mass is considerably smaller, and, hence, the velocity dispersion in S_1 remains lower than the others.

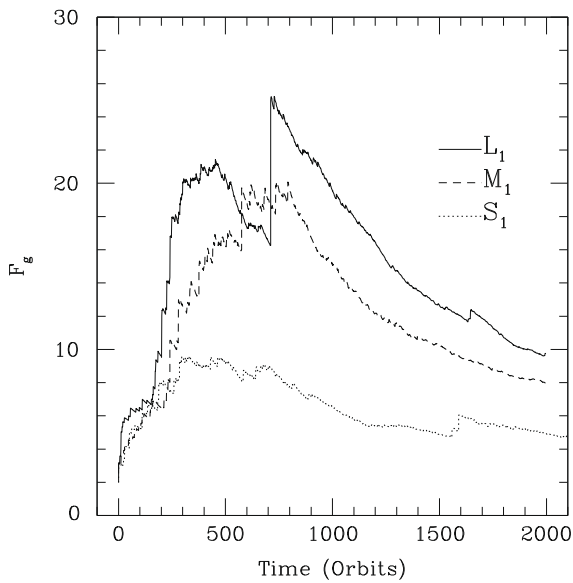


Fig. 27. Evolution of F_g as a function of time for the three baseline simulations.

In Fig. 27 we see the evolution of the three gravitational focusing factors in the baseline simulations. All appear to grow, reach a maximum, and then decrease. The peak is at about 300 orbits for S_1 and 600 for M_1 . The largest run L_1 is double-peaked, at 400 orbits and 700 orbits. The turnover at 400 orbits in L_1 may be a statistical fluke that is dramatically corrected at 716 orbits, or it may be that the turnover at 400 orbits is real, and that the event at 716 orbits is anomalous. The curves in Fig. 24 suggest the former. At $t = 200$ the largest particle in L_1 begins to grow significantly faster than the second largest, even though the two have approximately the same mass. Then at $t = 400$, the difference between the two begins to decrease suddenly. The two are almost identical at $t = 700$ when two large particle merge at 716 orbits. At this point, the largest particle once again becomes significantly larger.

In Fig. 28 we show the evolution of $e_{RMS}/\sin i_{RMS}$. After initially dropping from 2.35 (see Fig. 9), the value in L_1 remains close to 2.1

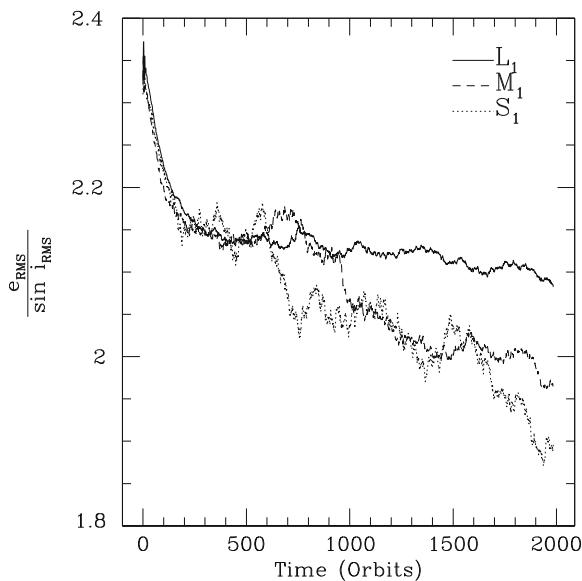


Fig. 28. The ratio of e_{RMS} to $\sin i_{RMS}$ as a function of time. The ratio in L_1 remains slightly over 2 for the duration of the simulation, but the ratio for M_1 and S_1 trends down.

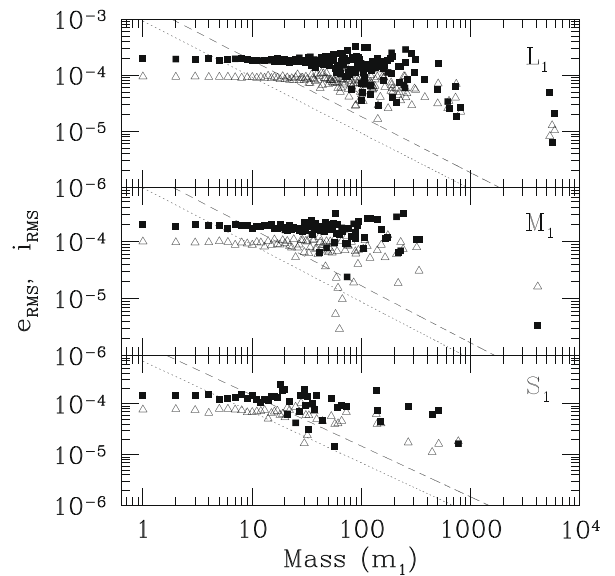


Fig. 29. The values of e_{RMS} and i_{RMS} as a function of mass at 2000 orbits for the three baseline simulations. Filled squares are eccentricity, open triangles are inclination. For reference, the dashed line represents equipartition of energy in e , dotted in i , normalized to values at $k = 10$.

for the duration of the simulation, suggesting the initial drop is a transient effect. However, in M_1 and S_1 , the evolution is steady from 200 to 600 or 900 orbits, respectively, and then appears to drop monotonically at later times. The overall drop represents about a 10% change.

In Fig. 29 we examine dynamical friction in the baseline runs at 2000 orbits. We saw in Fig. 10 that there was a general trend of decreasing velocity with increasing mass, although the slope of this trend is so shallow that kinetic energies trend higher with increasing mass. The same general pattern is seen at 2000 orbits for large masses ($m \geq 100m_1$), but velocity is independent of mass for smaller masses. Note as well that the mean values for the small-mass particles are larger at 2000 orbits than at $t_{1/2}$.

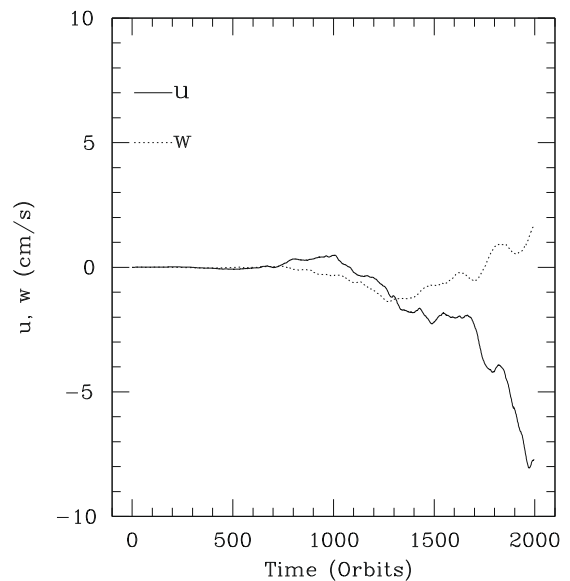


Fig. 30. Evolution of u and w in Simulation L_1 . The values grow quickly after the merger at 713 orbits.

Next we examine the validity of the L_1 patch from $t_{1/2} - 2000$ orbits. First we plot the evolution of u and w in Fig. 30. Both values remain small until the major merger event at 713 orbits. At that time, the values grow significantly, finally reaching $u = -7 \text{ cm s}^{-1}$, about two orders of magnitude larger than its value at $t_{1/2}$. This velocity means that the center-of-mass velocity is roughly $1/70$ the total shear across the patch, and that certainly by the end of the simulation our assumptions have broken down.

Next we look at how effective different mass bins are at stirring the patches at different times in Fig. 31. We saw in Fig. 14 that by $t_{1/2}$ the distribution of $m^2 N_k$ was flat, and in Fig. 31 we see that the slope is positive at all times after $t_{1/2}$ for all simulations. These positive slopes indicate that the patch is not large enough since very

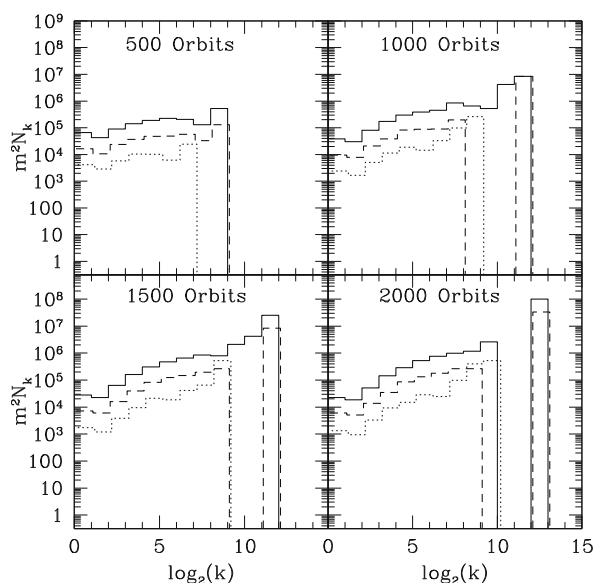


Fig. 31. Distribution of stirring power as a function of mass at four separate times in all baseline simulations. By the end of the simulation, each of the three largest particles in L_1 (solid line) are an order of magnitude more effective at stirring the patch than all the other particles combined. Note that the Simulation M_1 data (dashed line) are offset by 0.1 and the S_1 data (dotted line) by 0.2.

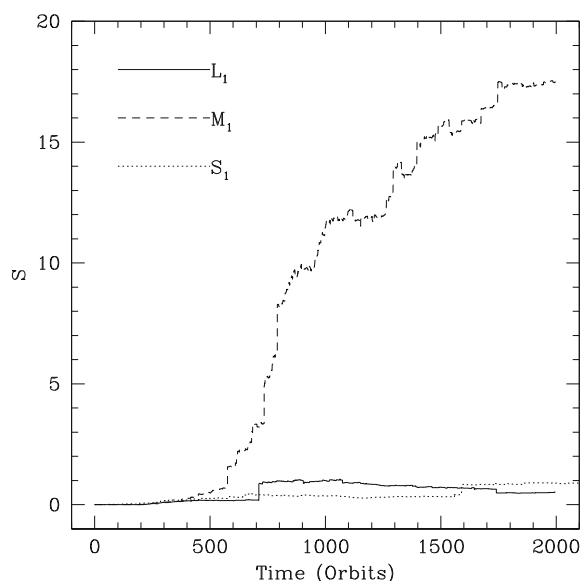


Fig. 32. Evolution of S as a function of time for the three baseline models.

large particles not in the patch can substantially affect the velocity distribution in the patch (see Section 4.4.2).

Finally, we examine the value of S in Fig. 32. The value in L_1 stays below 0.15 until 713 orbits, indicating the largest-mass particle is not dominating the stirring in the patch. However, the merger at 713 orbits creates a particle whose stirring is about equal to the stirring of the sum of all other particles in the patch. Therefore at this point, the assumptions of the patch framework break down, and we cannot expect the simulation to be providing reliable results. As other large particles appear in L_1 , S slowly drops. In M_1 , the value nearly reaches unity at 700 orbits, and then grows quickly to a final value of 17.5. In S_1 , S remains below unity for the duration of the simulation, but note the sudden jump at 1600 orbits.

The results presented in this appendix reveal the numerous ways in which our patch model breaks down after $t_{1/2}$. The assumptions of small center-of-mass motion, no dominant mass inside the patch, and no outside perturbers have all failed in the three baseline models.

References

- Aarseth, S., Lecar, M., 1984. The formation of the terrestrial planets from lunar sized planetesimals. In: Brahic, A. (Ed.), Proc. to IAU Colloq. No. 75: Planetary Rings, Cepadues, Toulouse, pp. 661–674.
- Adachi, I., Hayashi, C., Nakazawa, K., 1976. The gas drag effect on the elliptical motion of a solid body in the primordial solar nebula. PThPh 56, 1756–1771.
- Agnor, C.B., Canup, R.M., Levison, H.F., 1999. On the character and consequences of large impacts in the late stage of terrestrial planet formation. Icarus 142, 219–237.
- Barnes, J., Hut, P., 1986. A hierarchical $O(N \log N)$ force-calculation algorithm. Nature 324, 446–449.
- Binney, J., Tremaine, S., 1994. Galactic Dynamics. Princeton University Press, Princeton, NJ, pp. 120–126.
- Chamberlin, T.C., 1901. On a possible function of disruptive approach in the formation of meteorites, comets, and nebulae. Astrophys. J. 14, 17–41.
- Chambers, J.E., 2001. Making more terrestrial planets. Icarus 152, 205–224.
- Edgeworth, K.E., 1949. The origin and evolution of the solar system. MNRAS 109, 600–609.
- Garaud, P., Lin, D.N.C., 2004. On the evolution and stability of a protoplanetary disk dust layer. Astrophys. J. 608, 1050–1075.
- Gehrels, N., 1986. Confidence limits for small numbers of events in astrophysical data. Astrophys. J. 303, 336–346.
- Goldreich, P., Ward, W.R., 1973. The formation of planetesimals. Astrophys. J. 183, 1051–1062.
- Goldreich, P., Lithwick, Y., Sari, R., 2004. Final stages of planet formation. Astrophys. J. 614, 497–507.
- Greenberg, R., Hartmann, W.K., Chapman, C.R., Wacker, J.F., 1978. Planetesimals to planets – Numerical simulation of collisional evolution. Icarus 35, 1–26.
- Greenzweig, Y., Lissauer, J.J., 1990. Accretion rates of protoplanets. Icarus 87, 40–77.
- Hayashi, C., 1980. Structure of the solar nebula, growth and decay of magnetic fields and effects of magnetic and turbulent viscosities on the nebula. PThPS 70, 35–53.
- Hayashi, C., Nakazawa, K., Adachi, I., 1977. Long-term behavior of planetesimals and the formation of the planets. PASJ 29, 163–196.
- Heggie, D.C., 1975. Binary evolution in stellar dynamics. Mon. Not. R. Astron. Soc. 173, 729–787.
- Hill, G.W., 1878. Researches in the lunar theory. Am. J. Math. 1, 5–26.
- Johansen, A., Oishi, J.S., Low, M.M., Klahr, H., Henning, T., Youdin, A., 2007. Rapid planetesimal formation in turbulent circumstellar disks. Nature 448, 1022–1025.
- Kenyon, S.J., Bromley, B.C., 2006. Terrestrial planet formation. I. The transition from oligarchic growth to chaotic growth. Astron. J. 131, 1837–1850.
- Kenyon, S.J., Bromley, B.C., 2004. Collisional cascades in planetesimal disks. II. Embedded planets. Astron. J. 127, 513–530.
- Kenyon, S.J., Luu, J.X., 1998. Accretion in the early kuiper belt. I. Coagulation and velocity evolution. AJ 115, 2136–2160.
- Kokubo, E.S., Ida, S., 1996. On runaway growth of planetesimals. Icarus 123, 180–191.
- Kokubo, E.S., Ida, S., 2002. Formation of protoplanet systems and diversity of planetary systems. Astrophys. J. 581, 666–680.
- Kolvoord, R.A., Greenberg, R., 1992. A critical reanalysis of planetary accretion models. Icarus 98, 2–19.
- Leinhardt, Z.M., Richardson, D.C., 2005. Planetesimals to protoplanets. I. Effect of fragmentation on terrestrial planet formation. Icarus 625, 427–440.
- Leinhardt, Z.M., Richardson, D.C., Lufkin, G., Haseltine, J., 2009. Planetesimals to protoplanets. II: Effect of debris on terrestrial planet formation. MNRAS 396, 718–728.

- Lissauer, J.J., 1987. Timescales for planetary accretion and the structure of the protoplanetary disk. *Icarus* 69, 249–265.
- Lissauer, J.J., 1995. Urey prize lecture: On the diversity of plausible planetary systems. *Icarus* 14, 217–236.
- Lissauer, J.J., Slartibartfast, 2008. How extreme can planets be? In: Fischer, D.A., Rasio, F.A., Thorsett, S.E., Wolszczan, A. (Eds.), *Extreme Solar Systems*, ASP Conference Series, pp. 491–498.
- Lissauer, J.J., Stewart, G.R. 1993. Growth of planets from planetesimals. In: Lissauer, J.J., Stewart, G.R. (Eds.), *Protostars and Planets III*, pp. 1061–1088.
- Moore, B., Governato, F., Quinn, T., Stadel, J., Lake, G., 1998. Resolving the structure of cold dark matter halos. *Astrophys. J.* 499, L5–L8.
- Morishima, R., Schmidt, M.W., Stadel, J., Moore, B., 2008. Formation and accretion history of terrestrial planets from runaway growth through to late time: implications for orbital eccentricity. *Astrophys. J.* 685, 1247–1261.
- O'Brien, D.P., Morbidelli, A., Levison, H.F., 2006. Terrestrial planet formation with strong dynamical friction. *Icarus* 184, 39–58.
- Press, W.H., Teukolsky, S.A., Vetterling, W.T., Flannery, B.P., 1996. *Numerical Recipes in C: The Art of Scientific Computing*. Cambridge University Press, Cambridge. pp. 657–661.
- Rafikov, R.R., 2004. Fast accretion of small planetesimals by protoplanetary cores. *Astron. J.* 128, 1348–1363.
- Raymond, S.N., Barnes, R., Kaib, N., 2006. Predicting new planets in known extra-solar planetary systems. III: Terrestrial planet formation. *Astrophys. J.* 644, 1223–1231.
- Richardson, D.C., Quinn, T., Stadel, J., Lake, G., 2000. Direct large-scale *N*-body simulations of planetesimal dynamics. *Icarus* 143, 45–59.
- Safronov, V.S., 1960. On the gravitational instability in flattened systems with axial symmetry and non-uniform rotation. *Ann. Astrophys.* 23, 979–982.
- Safronov, V.S., 1969. *Evolution of the protoplanetary cloud and formation of the Earth and the planets* (NASA Tech. Trans. F-677, Nauka Press, Moscow).
- Saha, P., Tremaine, S., 1992. Symplectic integrators for solar system dynamics. *Astron. J.* 104, 1633–1640.
- Stadel, J.G., 2001. *Cosmological *N*-body simulations and their analysis*. Ph.D. Thesis, University of Washington.
- Stewart, G.R., Wetherill, G.W., 1988. Evolution of planetesimal velocities. *Icarus* 74, 542–553.
- Wadsley, J.W., Stadel, J., Quinn, T., 2004. Gasoline: A flexible, parallel implementation of TreeSPH. *New Astron.* 9, 137–158.
- Weidenschilling, S.J., 1977. Aerodynamics of solid bodies in the solar nebula. *Mon. Not. R. Astron. Soc.* 180, 57–70.
- Weidenschilling, S.J., 1995. Can gravitational instability form planetesimals? *Icarus* 116, 433–435.
- Weidenschilling, S.J., Cuzzi, J.N., 1993. Formation of planetesimals in the solar nebula. *Protostars and Planets III*, pp. 1031–1060.
- Weidenschilling, S.J., Spaute, D., Davis, D.R., Marzari, F., Ohtsuki, K., 1997. Accretional evolution of a planetesimal swarm. *Icarus* 128, 429–455.
- Wetherill, G.W., 1990. Comparison of analytical and physical modeling of planetesimal accumulation. *Icarus* 88, 336–354.
- Wetherill, G.W., Stewart, G.R., 1989. Accumulation of a swarm of small planetesimals. *Icarus* 77, 330–357.
- Wisdom, J., Tremaine, S., 1988. Local simulations of planetary rings. *Astron. J.* 95, 925–940.
- Youdin, A.N., Shu, F., 2002. Planetesimal formation by gravitational instability. *Astrophys. J.* 580, 494–505.